TOWARDS THE FABRICATION OF BIORESORBABLE CONSTRUCTS WITH

CUSTOMIZED PROPERTIES USING ADDITIVE MANUFACTURING

by

PRASHANTH RAVI

Presented to the Faculty of the Graduate School of

The University of Texas at Arlington in Partial Fulfillment

of the Requirements

for the Degree of

DOCTOR OF PHILOSOPHY

THE UNIVERSITY OF TEXAS AT ARLINGTON

December 2017

Arlington, Texas

Supervising Committee:

    Panos S. Shiakolas
    Tre R. Welch
    Pranesh B. Aswath
    Venu G. Varanasi
    Seiichi Nomura

I can't help but mention that science is really a collaborative project, and I feel very fortunate to have had the opportunity in life to add a tiny drop to the ocean of human knowledge with this dissertation. My sincere gratitude also to the University of Texas at Arlington for the financial support and for providing an environment conducive to learning. My sincere wish is to stay in touch and give back to this great institution from which I have gained so much.

Last but certainly not the least, my biggest thanks to my parents for giving me the freedom to pursue my ambitions relentlessly. And finally, thanks to my brother Dr. Chaitanya Ravi, conversations with whom have made me a better version of myself and were the single biggest motivation in pursuing doctoral education.

November 15, 2017

Abstract

TOWARDS THE FABRICATION OF BIORESORBABLE CONSTRUCTS WITH

CUSTOMIZED PROPERTIES USING ADDITIVE MANUFACTURING

Prashanth Ravi

The University of Texas at Arlington, 2017

Supervising Professor: Panos S. Shiakolas

Additive Manufacturing (AM) has been employed to fabricate medical constructs for over two decades. This dissertation investigates the effects of AM process parameters on raster level geometric features and structural properties of bioresorbable constructs. The development of an open architecture custom multi-process 3D printer employed for fabricating bioscaffolds and test structures is discussed. Bioresorbable polymers including a newly synthesized radiopaque polymer, poly (glycerol sebacate fumarate) gadodiamide (Rylar) and medical grade poly-L-lactic acid (PLLA) were investigated. In the first part, the effects of process parameters on raster geometry were investigated to aid in the fabrication of structures with improved geometric features using Fused Filament Fabrication (FFF). In the second part, the effects of FFF laydown patterns on PLLA scaffold degradation in PBS were studied. In the third part, a UV *in situ* photopolymerization module was developed, integrated with the in-house 3D printer, and used to investigate the effects of process parameters on the structural and thermal properties of Rylar constructs using a dynamic mechanical analyzer. Design of Experiments was employed to analyze the effects of process parameters on the properties. Predictive models were developed and verified using randomly selected process parameter levels. The developed AM procedures could be employed to fabricate customized bioconstructs with desired functionality for specific soft and hard tissue applications such as tracheal airways and bones, respectively.

Table of Contents

List of Illustrations

x

List of Tables

Chapter 1

INTRODUCTION

1.1 Additive Manufacturing Basics, Technologies and Applications

Additive manufacturing (AM) or 3D printing refers to the layer-by-layer or bottom-up fabrication of an object from a CAD model[1]. This contrasts with the conventional subtractive or top-down manufacturing scheme wherein a desired object is fabricated by removing material from a larger workpiece. A schematic capturing the sequence of steps for common AM techniques is given in Figure 1, where the marked steps are often optional. First, a 3D CAD model of the desired object is created and converted to the Standard Tessellation Language (STL) file format, where it is described as an unstructured triangulated surface with vertices and unit normal in a 3D Cartesian coordinate system. The STL file is later imported into a slicing package such as Slic3r, Simplify3D, Cura, etc. where the tool path settings are defined prior to generating motion commands typically in the form of G-codes adapted for AM. Although rarely needed, sometimes the generated G-codes need to be modified to fulfill additional requirements which the slicing package may not support. The motion commands are then sent to the process control card line-by-line to 3D print the desired object via an interfacing software such as Repetier-Host which also monitors important process related parameters including extruder temperature and axes limits among others. Depending on the AM process used for fabrication, once the object has been 3D printed it might need post-processing such as immersion in a bath for removal of support material, heat-based treatments or other processes to enhance or introduce desired features or other finishing operations.
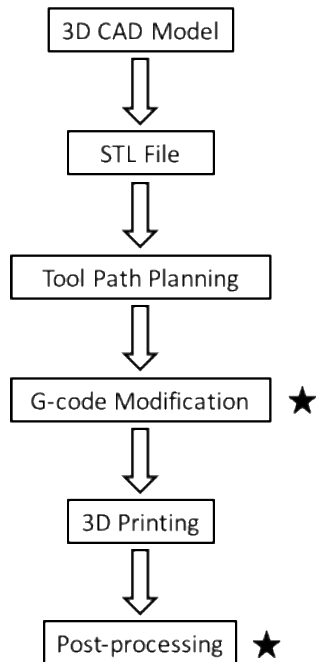
Figure 1. Generalized schematic for the sequence of steps in AM processes.

3D printing in the form of the Stereolithography Apparatus (SLA) was invented in the 1980s by Charles Hull while he was curing resins for tabletop coatings[2]. Since then, a variety of 3D printing technologies such as Fused Deposition Modeling (FDM)/Fused Filament Fabrication (FFF), Robocasting/Direct Ink Writing (DIW), inkjet-based Bioprinting, powder-binder based 3D printing (3DP), Selective Laser Sintering (SLS), Electron Beam Melting (EBM), and Continuous Liquid Interface Production (CLIP) have been invented to cater to specific niche applications[3–8]. AM technologies have dramatically revolutionized the manufacture of industrial components over the past three decades, and tissue engineering scaffolds in the biomedical domain over the past two decades. The layer-by-layer or bottom-up fabrication style utilized in 3D printing allows a user to prototype a designed object with intricate features in a relatively short time period without the need to develop part specific tooling or dies[9–11]. Because the transition from designed object to

manufactured part is relatively straightforward without complicated constraints, it opens the door to customize intricate features at the design-level using techniques such as topology optimization. Alternatively, features and properties in the final component can also be tailored by customizing settings during the tool path planning (slicing) process which can be referred to as customization-by-process[12–18]. It is therefore easy to visualize how 3D printing has the potential to transform the way components are both designed and manufactured. For example, in the case of low volume manufacturing of components with highly complex geometries, 3D printing becomes the obvious manufacturing choice since the tedious process of developing customized tooling, dies or molds is automatically eliminated. Similarly, several iterations usually take place in any design process, and 3D printing is a perfect ally for conducting multiple iterations in a speedier manner. A newer development in 3D printing includes multi-material or hybrid 3D printing wherein multiple processes are combined onto a single platform to fabricate components such as printed circuit boards (PCBs) that typically require multiple processes to successfully manufacture.

1.2 Literature Review and Challenges

Conventional approaches such as freeze drying, salt leaching, phase separation, and electrospinning do not allow for the highly reproducible and controllable fabrication of biomedical scaffolds (bioscaffolds) with desired properties such as pore structure shape, size and interconnectivity[19–23]. Moreover, such techniques frequently demand specialized tooling/dies, and often result in structures with poor and unpredictable mechanical properties[24]. Solid freeform fabrication (SFF) techniques have gained widespread usage owing to their layer-by-layer manufacturing capability and documented reproducibility[25–31]. Commercially available setups such as the BioScaffolder (Analytik Ltd.), the 3D-Bioplotter (ENVISIONTEC Inc.) and the NovoGen MMX Bioprinter (Organovo Inc.) integrate several

pneumatic syringe-based dispensing heads with or without a high temperature polymeric head to extrude multiple pasty materials. However, most of the commercial setups utilize proprietary processing algorithms and software to drive their respective setups. Moreover, many of the setups are resource intensive and therefore beyond reach for most end-users as well as researchers. Therefore, to enable research using new biomaterials as well as to allow customization of hardware, we developed a modular AM system in-house that is controlled using open source software thus rendering findings from the research more accessible and reproducible.

Several investigators have studied the effects of AM process parameters on the overall features of fabricated components such as surface roughness, build time, dimensional accuracy and mechanical properties using Design of Experiments (DoE) and Artificial Neural Network (ANN) based techniques[12,13,32–38]. However, very few investigators have focused on the effects of AM process parameters on raster-level features such as width, height, morphology etc. This is essential since an AM component is ultimately a collection of individual rasters, and a better control over raster-level features could drastically improve the overall properties of fabricated components. Moreover, although a few reports can be found addressing researching discussing design-based optimization and 3D printing of structures with defined features, success is generally moderate to low using such techniques partly due to AM constraints that are unaccounted for[39,40]. However, a process-based optimization by appropriate adjustment of process parameters is more readily implementable for the end-user with high success rate, although the downside is that the development of an empirical predictive model requires moderate to extensive experimentation for data collection and analysis[41]. For example, the Young's modulus of a photocrosslinked structure can be finely tailored by adjusting the UV exposure time,

however, accurately measuring this property requires additional testing equipment beyond the 3D printer such as a dynamic mechanical tester or tensile machine.

Detailed reports of 3D printing for tissue engineering applications using medical grade or bioresorbable materials are still relatively limited in the open literature. For example, most scaffold type structures are 3D printed using thermoplastic polymers such as amorphous poly lactic acid (PLA) or poly caprolactone (PCL). 3D bioprinting using PCL is relatively straightforward due to the low melting temperature compared with PLA, which is not as harmful to living cells. Furthermore, even fewer reports on multi-material AM of bioresorbable structures using 2 or more materials exist in the literature. Multi-material 3D printing can be leveraged to fabricate structures with advantageous properties pooled from individual materials, which is otherwise not possible using single material fabrication. For example, PLA which is a rigid thermoplastic polymer can be used to provide integrity to the structure, whereas a more viscoelastic polymer such as poly ethylene glycol (PEG) with better biomaterial-cell interaction properties could be used to 3D print the outer layers to improve overall performance *in vivo*. Such a combination of properties is difficult to achieve with only a single material despite using design-optimization techniques to optimally distribute material inside the structural matrix, since it is still the same material unless design-optimization using multi-materials is implemented to introduce true material heterogeneity. Therefore, the present dissertation seeks to investigate the effect of AM process parameters on raster-level features and overall mechanical properties of structures 3D printed using novel bioresorbable materials in an effort to bridge the existing knowledge gap in those areas.

1.3 Dissertation Aims

The specific aims of the dissertation research are presented below in bullet form:

1. Provide a detailed description of the in-house development of an open architecture 3D printing platform.

2. Study the effect of FFF process parameters on raster-level geometric features.

3. Investigate the effect of AM process parameters on the properties of homogeneous structures 3D printed using novel bioresorbable materials: medical grade PLLA and a bioresorbable resin poly (glycerol sebacata fumarate) gadodiamide (PGSFGdA) henceforth referred to as Rylar.

4. Undertake a preliminary investigation to assess the 3D printability of true composite-type structures using a combination of PLLA and Rylar biomaterials.

1.4 Dissertation Overview

This document is an article-based dissertation with chapters 2-5 being refereed conference/journal publications fulfilling the aims set out.

- Chapter 1: AM basics, common AM technologies and some known applications are discussed in the Introduction section. A literature review with existing challenges as they relate to the dissertation is presented. Finally, a brief summary of contributions is provided with an overview of the dissertation.

- Chapter 2: A detailed description of the in-house AM platform development is provided (Aim 1) based on refereed conference papers published in the proceedings of the 2015 American Society of Mechanical Engineers (ASME) International Mechanical Engineering Conference and Exposition (IMECE).

- Chapter 3: A DoE study investigating the effect of the nozzle temperature and nozzle-bed distance process parameters on strut width (Aim 2) was undertaken. The data was used to develop a multi-linear regression model to predict width of

rasters and fabricate single-layer scaffolds with defined spacings between rasters (pore sizes). 3D printing commercial grade PLA was used due to the low diameter dimensional variation of the filament compared with in-house fabricated medical grade PLLA filament. The chapter is based on an original research article published in the 2017 ASME Journal of Manufacturing Science & Engineering volume 139 and issue 7.

- Chapter 4: Medical grade poly-L-lactic acid (PL-32) pellets were extruded into filament for 3D printing scaffolds with 4 distinct infill patterns. The effect of infill pattern on scaffold weight loss was assessed (Aim 3). Melt rheometric data of the polymer was obtained and analyzed showing pseudoplastic behavior. The process parameters were set based on rheometric data and scaffolds weights were recorded for six months. Although statistically significant differences were not found between the 4 infill patterns, distinctive temporal trends in weight loss were observed corresponding to different infill patterns. The chapter is based on an original research article published in the August 2017 Elsevier Additive Manufacturing Journal volume 16.

- Chapter 5: Poly (glycerol sebacate fumarate) gadodiamide, a newly synthesized biocompatible bioresorbable photo- and thermally curable resin, was used to study the effects of UV intensity and print speed (exposure time) on the properties of 3D printed structures (Aim 3) such as Young's modulus (E), ultimate tensile strength (UTS), failure strain, toughness, and glass transition temperature (T_g). Strong correlation was observed between the process parameters and the responses for the material properties. A regression model was developed and experimentally verified predicting Young's modulus with a respectable level of accuracy. The mechanical properties showed good agreement with human tracheal tissue and

other soft polymeric structures. The chapter is based on an original research article currently under review with the Journal of Biomedical Materials Research Part B. The Appendix section of the chapter (unpublished) briefly discusses preliminary observations and findings from the fabrication of a composite PLLA and Rylar-PEGDA disk as a stepping stone for a hybrid tracheal splint (Aim 4).

- Chapter 6: A summary of the dissertation research is provided followed by some conclusions and specific recommendations for future research.

Chapter 2

ON THE DEVELOPMENT OF A MODULAR 3D BIOPRINTER FOR RESEARCH IN

BIOMEDICAL DEVICE FABRICATION[1]

Authors: Prashanth Ravi, Panos S. Shiakolas, Jacob C. Oberg, Shahid Faizee and Ankit K. Batra.

Author Contributions: PSS and JCO conceived the modular bioprinter. PSS, JCO, PR, AKB and SF contributed to the bioprinter design, development, testing, calibration and fabrication of test structures. PR prepared the manuscript which was later critically revised by PSS.

Link to access the full peer-reviewed and published paper: http://proceedings.asmedigitalcollection.asme.org/proceeding.aspx?articleid=2500426.

---

[1] Used with permission of the American Society of Mechanical Engineers, 2017.

2.1 Abstract

Biomanufacturing research involving solid freeform fabrication techniques has become fairly widespread in recent times. The layer-by-layer building style offers an opportunity for developing a modular 3D printer to broaden the scope of biomanufacturing research. In this work, a Custom Multi-Modality 3D Bioprinter (CMMB) was conceived, designed and developed in the MARS lab at the University of Texas at Arlington (http://mars.uta.edu/). Currently, the hardware of the printer includes two Fused Filament Fabrication (FFF), one Photo Polymerization (PP), Viscous Extrusion (VE) and Inkjet (IJ) modules. The development of the custom bioprinter and each module are discussed; focusing on the advantages of a modular design, and on the unique features present in each individual module. Select constructs fabricated using individual or a combination of modules are introduced. Design of Experiments (DOE) principles employing Design Expert statistical software were used to characterize the CMMB; interactions between fabrication process parameters, and their effect on deposited strand characteristics were analyzed. These results were used to improve the quality of subsequently fabricated constructs. Initial experiments and fabricated constructs demonstrate that the custom bioprinter is a novel CAD-CAM biomanufacturing platform for researching methodologies, materials and processes for the fabrication of biomedical devices.

2.2 Introduction

Biofabrication relies heavily on the integration of knowledge from several disciplines including engineering, biomaterials science, cell biology, physics and medicine[5]. Currently, one of the many challenges facing biofabrication is the ability to print using multiple freeform fabrication technologies and material types on a single fabrication platform without

losing positional calibration. Researchers have been able to successfully fabricate biological constructs by adapting personal inkjet printers[21,42–44] and by controlled extrusion of hydrogels[45–48]. Some have also been able to adapt multiple actuation mechanisms for fabricating constructs using various biopolymers[28]. Success has also been achieved with the integration of syringe based heated polymer deposition and controlled viscous extrusion technologies[27,49–51], with photo-crosslinking[52]. One of the significant disadvantages of constructs printed using inkjet and viscous extrusion (also know widely as micro extrusion) technologies is low structural integrity[53], along with the inability to print removable supports for constructs with overhangs[54]. Moreover, easy customization of mechanical properties in the printed scaffold is very difficult mainly due to the unavailability of processing software for generating customized tool paths. To address this shortcoming, some researchers chose to develop their own custom software to process a solid model and generate tool paths to deposit material[50,55–57].

An ideal Computer Aided Design (CAD) based motion control software must enable seamless control over available 3D printing modalities, in a way that ease of user operation is maintained, without compromising the important aspect of tailorability of features in the fabricated construct. The principal objective was to fulfill the goal of printability of biological constructs by combining advantageous features that are unavailable from any single technology. The open source 3D printing movement has accelerated collaboration between software developers, allowing them to develop robust and easily customizable processing software; thus enabling the fabrication of high quality 3D printed components. The custom 3D bioprinter discussed in this work utilizes the software Slic3r (http://Slic3r.org/), to slice 3D models and generate tool paths to deposit material at appropriate locations during printing. From the perspective of biomedical implant fabrication, Slic3r provides customizability of important physical features of the

construct such as porosity, slicing height, and strand width. The principal disadvantage of using Slic3r is that generated G-codes must subsequently be post-processed for incorporating multiple modules; which is a fairly laborious process that could be eliminated with the development of a customized version of Slic3r, which will allow the seamless integration of available technologies.

In this research, the development and successful demonstration of a multi-modality multi-material 3D BioPrinting platform is presented. The principal motivation behind developing the CMMB was to adapt advantageous hardware and software features from established freeform fabrication technologies onto a single platform for enhance and improve bio-fabrication research[5]. The CMMB incorporates fabrication technologies (modalities) including Fused Filament Fabrication (FFF), Viscous Extrusion (VE), Photo Polymerization (PP), and Inkjet (IJ). This additive manufacturing environment provides the ability to print different materials including biopolymers, gels, resins and ink, thus enhancing the scope and research potential involving a combination of such materials and fabrication technologies. The ability to customize the control process parameters such as operating temperature (T), nozzle-bed distance (NBD), print speed (PS), extrusion width (EW), infill density (ID) or pulsing frequency (PF) (depending on the module employed), in order to control print properties like porosity, pore size, etc. is important from the perspective of biomedical implant fabrication research since these properties have an impact on scaffold performance[20,25,56].

In order to understand interactions between the fabrication process parameters and their impact on printed strand characteristics obtained using the CMMB, experiments were performed and results analyzed statistically using the software Design-Expert from Stat-Ease Inc. Statistical results were employed to improve performance during subsequent prints. Initial experiments and fabricated sample constructs validate that the

CMMB has potential applications in customized scaffold fabrication, owing to the modular design and ability to integrate any of the available modalities in a single fabrication session.

2.3 The Concept of Modularity

The concept of modularity as used in this work refers to distinct printing heads (of the same/different processing technologies), i.e. a printing head which can be independently commanded to controllably dispense corresponding material at the appropriate location. From the initial design stage, the idea was to have a modular expandable environment and provide easy accessibility to hardware. Therefore, although the current setup of the CMMB includes two FFF modules and one module each of PP, VE, and IJ, it can be easily expanded to include upto six FFF modules and upto a combined total of four PP, VE and IJ modules in any combination. In addition, it was decided to use software tools that are both open source and versatile in terms of their functionality to produce tool paths for additive manufacturing (3D printing). It is postulated that this capability of easy expansion of hardware coupled with features present in the open source software tools (Slic3r and Repetier-Host) will allow incorporating different materials during fabrication of a single construct, thus changing the way constructs are typically fabricated using a bioprinter. The following sections further introduce each of the other FFF, PP, VE and IJ modalities on the CMMB and discuss their important and unique features. The currently available modalities along with biomaterial substrates and controllable process parameters for each modality are presented in Figure 2.
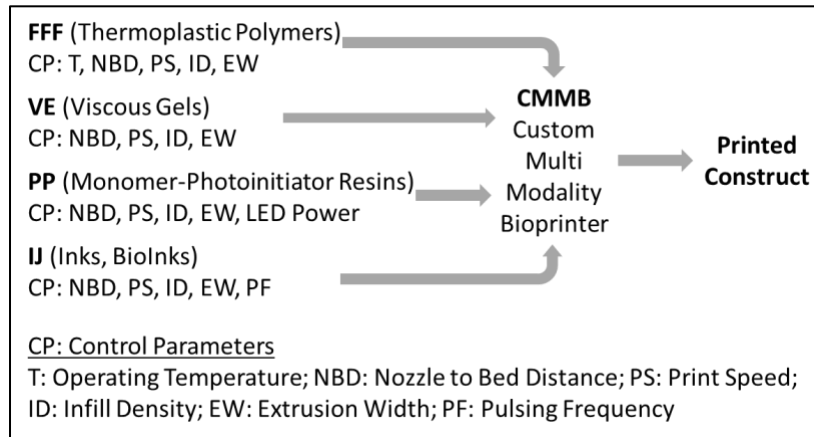
Figure 2. Block Diagram of the CMMB with material substrates and controllable process parameters for each module.

The NBD, PS, ID, and EW are parameters of interest that are controllable in Slic3r and are common across all modalities. Therefore, tool paths generated by the software Slic3r are directly employed (subsequent to post-processing for engaging specific modules/a combination of modules) for fabrication. LED power is controlled by adjusting the supplied voltage and the PF is adjusted by means of an Arduino-Shield IJ driver (Figure 3A) which is separately pre-programmed to energize the thermal micro-heaters on the HP inkjet print cartridge C6602A (black) at the desired rate. It is important to control the PF according to the PS to obtain appropriate properties in the resulting construct.

2.4 Development and Current Setup of the Custom Multi-modality Bioprinter (CMMB)

The CMMB was developed by the transformation of an existing micro router, into an additive manufacturing platform shown in Figure 3 and Figure 4. RUMBA process control card (http://www.reprapdiscount.com/electronics/33-rumba-basic-board.html) was used to send motion commands to the stepper motors, send power signals to the heater, receive signals from the thermocouples and send digital output signals as needed (Figure 5). The open source software Repetier-Host and Slic3r were utilized to interface with the printer for

fabrication purposes. The resolution of the motion platform is 0.003mm in the X, Y and Z directions. DRV8825 stepper motor drivers with 1/32 microstepping were used. Marlin firmware was customized to integrate available print modalities.
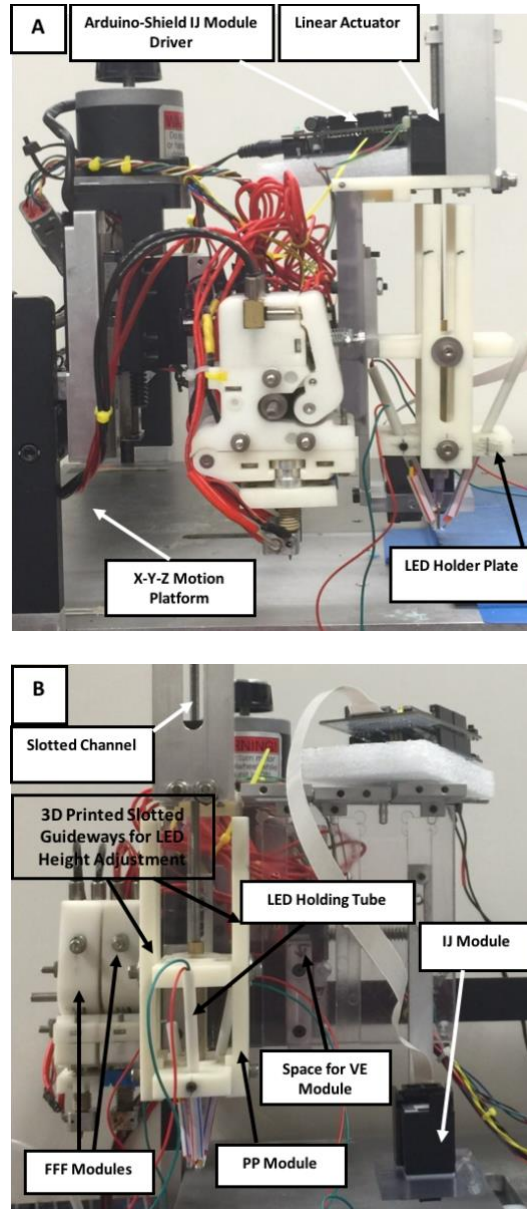
Figure 3. (A) Side view and (B) Front view of the Custom Multi-Modality 3D Bioprinter (CMMB).
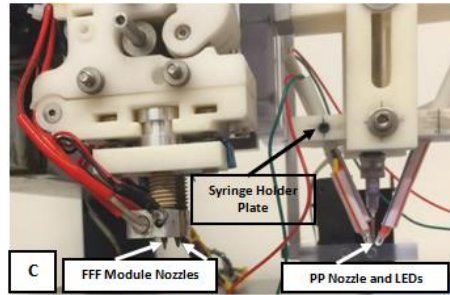
Figure 4. (C) Enlarged side view.
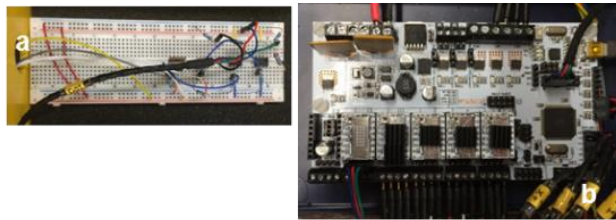
Figure 5. (a) Prototyped Opto-isolator circuit for engagement/disengagement signals (left) and (b) Rumba process control card (right).

2.4.1 Fused Filament Fabrication (FFF) Module

FFF is the most widely known and used 3D printing technology; also commonly known by the name Fused Deposition Modeling (FDM). FFF involves heating of a plastic filament which is subsequently pushed through a nozzle, and the resulting extruded strand is laid down in predefined paths to build an object layer-by-layer. The heater is controlled by the RUMBA process control card using a PID controller with gains defined using the Ziegler-Nichols procedure. The final fabricated part is mechanically rigid with excellent structural integrity; one of the many advantageous features in the FFF printing technology. In the CMMB, a few modifications were made to adapt the FFF technology for medical device fabrication research. Firstly, a provision is included for ease of calibration of the nozzle-bed distances (Figure 6). Secondly, a pressure-based solenoid actuation mechanism was

incorporated for engagement/ disengagement of multiple FFF modules on a single feeder motor.
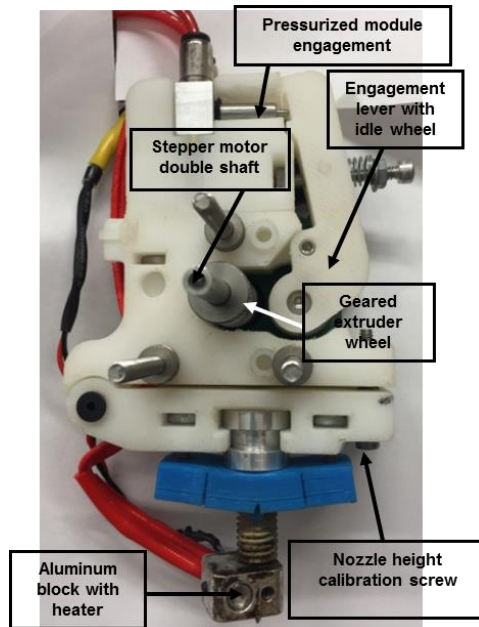
Figure 6. Fused Filament Fabrication (FFF) module with important components and unique features.

2.4.2 Inkjet (IJ) Module

Thermal inkjet printing modules have been used in several research studies to controllably dispense cells. Due to the established track record of previous studies, the IJ module was incorporated in the CMMB in order to provide the potential to deposit cells in the form of "bio-ink" in conjunction with the FFF, PP and VE modules. Micro-heaters in the thermal inkjet head cartridge have been successfully demonstrated to not cause significant damage to cells during the printing process; therefore they are deemed compatible for use in controlled dispensation of bio-ink[5]. Moreover, the IJ module on the CMMB has the capability to be independently calibrated easily due to the presence of slotted guide-ways (Figure 7); independent height calibration is important in order to properly integrate multiple

print technologies during a single print session to maintain constant nozzle-bed distance within each module.
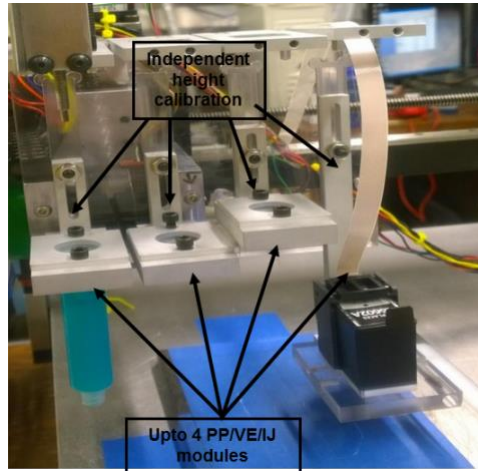
Figure 7. Independent calibration for the PP/VE and IJ modules due to machined slotted guideways.

2.4.3 Photopolymerization (PP) Module

Photopolymerization is a phenomenon in which a monomer, in the presence of a photoinitiator, undergoes crosslinking which changes its mechanical and chemical properties subsequent to ultraviolet (UV) light exposure from a laser, LED or other source. Photo-initiators are compounds that when exposed to UV light decompose into reactive species (free radicals) that initiate polymerization. For proper solidification of liquid polymer gel/resin, exposure to UV light at a particular wavelength is required in addition to exposure for a certain interval of time depending on the type of polymer and photo initiator.

The PP module consists of several 3-D printed components assembled together on the CMMB, Figures 2 & 3. The operation of the module involves two major steps: 1) engagement of the linear stepper motor which controllable advances the plunger to extrude the desired liquid monomer/ resin from the syringe nozzle, and 2) the on/off power to the LEDs for crosslinking of extruded resin. Step one was performed by the RUMBA process

control card through motion command signals; and step two was performed by the RUMBA board through a digital signal to an opto-isolator circuit that powers the LEDs. There are three UV LEDs on the PP module along with an LED holder. The LED holder was designed to have the flexibility to incorporate multiple adapter blocks for guiding the LED holding tubes. Two slotted guideways connect the syringe plate and the LED holder and are used for height adjustment (Figure 3). The relative height adjustment ensures that all three LEDs focus on the point where resin is dispensed. The syringe holding plate (Figure 3 & Figure 7) height is also adjustable owing to the machined slotted guideways provided for all the PP, VE and IJ module mounts.

2.4.4 Viscous Extrusion (VE) Module

The VE module was developed for controllably dispensing viscous/gel type materials such as hydrogels, growth factors, conductive ink, etc. The precise placement of cells, growth factors and signaling agents at appropriate locations in a scaffold is key to their subsequent proliferation and growth. This is achieved by using stepper drivers with 1/32 micro-stepping capability allowing for dispensing of extremely low volumes of viscous/gel materials.

The module also has a provision for the independent calibration of nozzle-bed distances through the utilization of slotted guide-ways similar to the PP and IJ modules (Figures 2 & 6). A standard syringe with an inner diameter of 9mm was used in the VE module. Syringe tip (needle) of 0.4mm diameter was used for initial experimentation.

2.4.5 Rumba Process Control Card Firmware: Marlin

For the CMMB, the firmware is where all the functions and subroutines necessary for the operating software Repetier-Host to interface with the 3D printer are defined. A modified version of the Marlin firmware (for bioprinting i.e. cold extrusion applications) was obtained from GitHub and modified to seamlessly incorporate multiple FFF modules onto a single

filament feeder motor. The firmware is currently modified by defining the tool change commands to allow for the integration and use of available printing technologies. Extruder change commands (T0, T1, T2, etc.) were redefined (in the Marlin_main.cpp file) to switch between multiple FFF modules (using the same filament feeder motor) by engaging appropriate solenoid valves using digital output signals from the RUMBA process control card. T0/T1 tool change commands were set to engage the two corresponding FFF modules one at a time, whereas T2 was defined to activate one of the other modules in the modified firmware. The number of tool change commands (currently at 3 including T0, T1 and T2) can be easily increased further in the firmware based on the available number of printing technologies in the CMMB. Finally, the file containing motion parameters which ensure compatibility with the printer hardware (the Configuration.h file) was modified by setting the axis steps per millimeter, the X-Y-Z travel limits, maximum velocity, acceleration and jerk.

2.4.6 Operating Software: Slic3r And Repetier-Host

Sli3r is an open source software that converts a 3D solid model into printing instructions (industry standard G-codes for the printer). Sli3r has several advantageous features from the perspective of scaffold based medical device fabrication research, including the capability to create custom infill patterns (rectilinear, honeycomb, angled rectilinear, concentric, Archimedean chords, octagram-spiral and Hilbert-curve) with controllable porosities (i.e. infill percentages), which are important factors for the success of a scaffold post implantation (Figure 8a). Sli3r is configurable for generating G-codes according to the size of nozzle used, which improves the fabrication scope of the CMMB. A major disadvantage of Slic3r is the inability to select distinct extruders (print technologies) to print distinct layers. To overcome this drawback, post-processing of G-codes is being performed. It is postulated that a permanent solution to overcome this challenge will involve

20

customizing Slic3r (or a similar software) in order to allow seamless integration of the FFF, PP, VE and IJ technologies on the same layer or same printed construct.

Repetier-Host is an open source 3D printing software and is the main driving software for interfacing with the CMMB (Figure 8b). G-codes generated by Slic3r are sent line by line to the RUMBA board using Repetier-Host. Temperature feedback information from the thermocouples of the FFF modules and endstop limit switches for the X, Y and Z stages are collected and processed by Repetier-Host. Advantageous features of Repetier-Host include the ability to send manual motion commands (G-codes), heating/ cooling commands (M-codes), pause signals to the printer, and an accurate 3D visualization of the .STL solid model and print bed for proper object placement, orientation and scaling among many others.
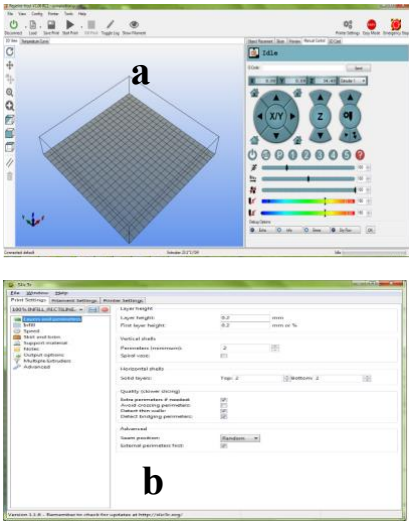
Figure 8. Open software (a) Repetier-Host and (b) Slic3r for tool path generation.

2.5 Characterization of Process Parameters

Preliminary experimentation indicated that three controllable process parameters, temperature, nozzle-to-bed distance, and print speed affect strand width, size and quality. Three distinct numeric levels were set for each parameter within the appropriate range in the experimental design for performing a full three-level-factorial Design of Experiments (DOE) statistical analysis using Design-Expert software (Stat-Ease Inc). The appropriate range for parameters that were selected based upon observations from preliminary fabrication runs were as follows: temperature was varied between 180℃ to 200℃, nozzle-bed distance between 0.150mm to 0.250mm and print speed between 200mm/min to 600mm/min. The temperature range was selected from 180 to 200℃ to be above the melting point of PLA (178℃); the nozzle-bed distance was varied between 0.15 to 0.25mm to be sufficiently lower than the nozzle diameter (0.5mm) and ensure good adhesion of printed strand with the bed, and the print speed was varied between 200 to 600mm/min for

evaluating the impact of print speed on strand width and to be lower than the maximum

allowable printing speed of 600mm/min (due to hardware considerations).
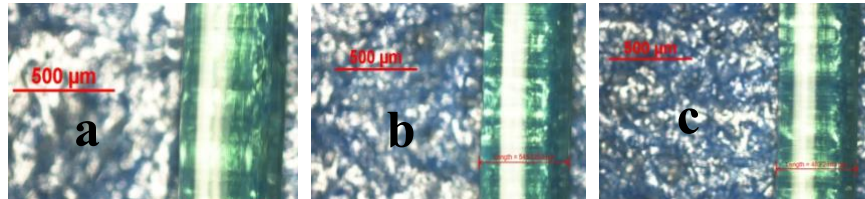
Figure 9. Digital bright field microscopic images obtained using Nikon Eclipse LV 150 microscope and NIS-Elements software showing (a) width of 495 microns (start), (b) 545 microns (center) and (c) 483 microns (end) for a 100mm long strand printed using PLA filament and the FFF module.

The printed PLA strand widths were measured using a digital microscope and

entered into Design-Expert for statistical analysis. The interactions between controllable

process parameters and their combined as well as individual effect on the resulting strand

widths were studied using ANOVA. Shown in Figure 9 is a digital microscopic image

showing the start, center and end strand widths printed using PLA filament and a single

FFF module on the CMMB with a nozzle of 0.500mm or twice the nozzle-bed distance,

temperature at 200ºC, nozzle-bed distance at 0.250mm and print speed at 200mm/min.

Figure 10 shows a surface plot at a constant temperature of 190˚C obtained from Design-

Expert; demonstrating that when temperature is held constant at 190˚C, the deviation in

the strand width is ±0.015mm from the mean. Therefore, the temperature was set at 190℃

for all subsequent fabrication runs. The temperature was maintained at 190$\pm$0.1℃ by

appropriately adjusting the PID gains in the firmware using first the PID autotune M-code

and then via subsequent trial-and-error experimentation to restrict the temperature

variation to within ±0.1℃ while ensuring an optimum settling time for temperature of the

heater.
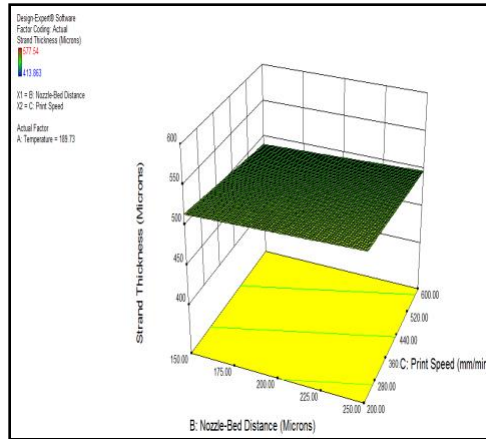
Figure 10. A 3D surface plot generated by the statistical software Design-Expert showing the effect of print speed and nozzle to bed distance on strand width (thickness). When the print temperature is maintained at 190˚C, the variance in strand widths is the lowest in the working range of the other two parameters.

2.6 Fabricated Construct: FFF Module

Figure 11 shows a 20x20mm^2 square shaped construct printed with alternating 0/90° rectilinear infill percentages; 80% ID in the top layer (layer 7), 30% ID in the layers 2-6 and 100% ID in the bottom layer (layer 1), printed with PLA polymer on a single FFF module in one print session. Nozzle inner diameter was 0.5mm and total thickness of the fabricated construct was 2mm with NBD (and layer height) maintained at 0.3mm. No post-processing of Slic3r generated G-codes was performed.

Figure 11. A 20x20mm^2 construct with 0/90° rectilinear infill (80% ID top layer, 30% ID internal layers and 100% ID bottom layer) fabricated.

2.7 Fabricated Construct: Integrated FFF and VE Modules

Figure 12 shows a 20X20mm^2 square construct with a 1x1mm^2 square cross sectional internal channel fabricated using PLA and a single FFF module. The channel was filled using the VE module with gel after printing of the channel with the FFF module in the same print session. For proof of concept verification and initial experimentation, toothpaste was used as a biogel equivalent due to ready availability and inexpensiveness. The construct was fabricated with 100% ID (for a tight seal). The channel was only half sealed on top (to show the filled channel) by again using the FFF module subsequent to filling of the channel using the VE module. Post-processing of the Slic3r generated G-codes was performed for fabricating the construct using an integration of the FFF and VE modules during a single print session.
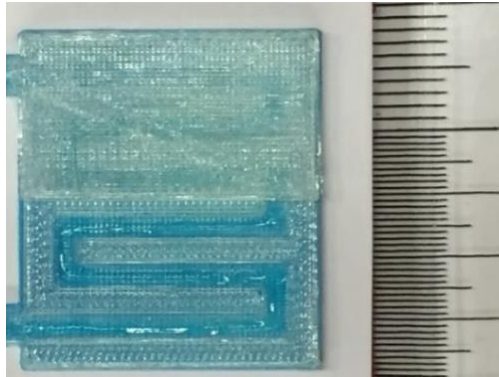
Figure 12. A 20x20mm^2 construct with a 1x1mm^2 internal channel fabricated using the FFF module and filled with toothpaste using the VE module.

2.8 Fabricated Patterns: IJ and VE Modules

Preliminary patterns were printed using the IJ and the VE modules (Figure 13 & Figure 14). These patterns were printed in order to test the operation of the IJ and VE modules. Post-processing of Slic3r generated G-codes was performed to energize the corresponding VE/IJ modalities in addition to modify the default extrusion axis, and setting the appropriate feeds using the volume conservation relationship.
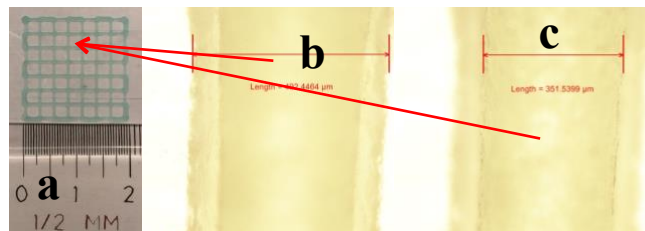
Figure 13. (a) A square 20x20mm^2 pattern with alternate 0/90° rectilinear 15% ID (2 layers). (b) Bottom layer strand (approx 0.480mm) and (c) top layer strand (approx 0.339mm) printed using Aim toothpaste with the VE module. Syringe tip was 0.4mm and sample was printed on regular A4 printing paper with 0.2mm NBD and 600mm/min PS.
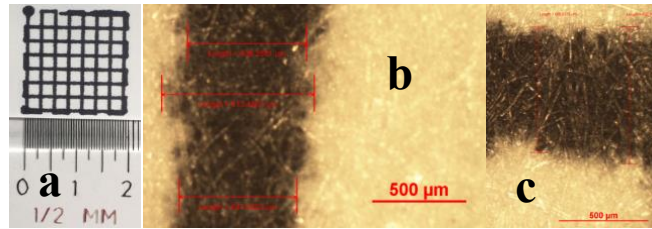
Figure 14. (a) A 20X20mm² pattern printed with alternate 0/90° rectilinear 15% ID pattern using the IJ module on regular A4 printing paper (1 layer). (b) 90° strand (approx 0.7mm) and (c) 0° strand (approx 0.7mm) printed using HP C6602a black cartridge. NBD was 0.2mm and PS was 600mm/min.

It is clear that the strand widths as seen in figures 8, 12 and 13 are much larger than the order of structural cues (<100µm) required by cells for proliferation in a tissue engineered scaffold. To address this challenge, a novel design of a nozzle for the FFF module is being investigated in order to allow the fabrication of strand with channels on the order of 100µm or lesser. Moreover, further investigation is needed to evaluate the use of smaller nozzle diameters with the FFF/VE and PP modules for increasing the printing resolution given that the X-Y-Z motion platform of the CMMB has a motion resolution of 0.003mm in the X, Y and Z directions (and therefore the lowest inter strand distance theoretically).

2.9 Conclusions, Challenges and Future Work

The purpose of this manuscript was to introduce the concept and advantages offered by a multimodality 3D printer and demonstrate successful design, development and initial application (through preliminary experiments and fabricated sample constructs) of the Custom Multi-Modality Bioprinter (CMMB) in the MARS lab at UT Arlington (http://mars.uta.edu/). We postulate that the custom bioprinter will aid in the fabrication of scaffold-based (using the FFF module) and scaffold-free (using the PP, VE & IJ modules) constructs. Principal advantages of the CMMB include the availability of established

material processing technologies in addition to the versatile open source driving software Slic3r and Repetier-Host. This provides the ability to integrate multiple materials as well as processing technologies in a single construct (within the same print session) without losing positional calibration.

Currently, one of the main challenges being faced with the CMMB is the inability to generate distinct layer-by-layer properties using multiple processing technologies without the need to manually post-process Slic3r generated G-codes. Another challenge is the adjustment of pulsing frequencies of the heating element in the inkjet head cartridge so as to be compatible with the movement speeds of the CMMB. In addition, the PP module needs to be characterized as well to understand the impact of controllable parameters on the polymerized strand width. These issues are being investigated further and results will be shared as the studies are completed.

An apriori knowledge of the material properties, in conjunction with initial experimentation and statistical analysis of obtained data will allow optimization of controllable parameters for each module utilized to print with the corresponding biomaterial of interest for fabricating the desired construct. One of the many challenges that the CMMB will be used to help address is in investigating the fabrication of a replacement heart valve (prosthetic/biological or hybrid) for pediatric patients born with congenital defects. It is postulated that the ability to combine different materials (including rigid polymers, viscous polymers/hydrogels, crosslinkable resins and bioink) in a single construct during the same print session, along with the ability to precisely tailor structural features in the construct will enable extensive experimentation which may eventually lead to the development of novel methodologies and material combinations for fabricating replacement valves.

2.10 Acknowledgments

Chapter 3

ANALYZING THE EFFECTS OF TEMPERATURE, NOZZLE-BED DISTANCE, AND

THEIR INTERACTIONS ON THE WIDTH OF FUSED DEPOSITION MODELED

STRUTS USING STATISTICAL TECHNIQUES TOWARD PRECISION SCAFFOLD

FABRICATION[2]

Authors: Prashanth Ravi, Panos S. Shiakolas and Avinash D. Thorat.

Author Contributions: PR and PSS conceived the project and designed the study. PR performed the experiments and took microscopic measurements. AD assisted with recording measurement data and statistical analysis. PR prepared the manuscript which was later critically revised by PSS.

Full Citation: Ravi, P.; Shiakolas, P. S.; Thorat, A. D. Analyzing the Effects of Temperature, Nozzle-Bed Distance, and Their Interactions on the Width of Fused Deposition Modeled Struts Using Statistical Techniques Toward Precision Scaffold Fabrication. *J. Manuf. Sci. Eng.* **2017**, *139* (7), 1–9.

Link to access the full peer-reviewed and published original research paper: http://manufacturingscience.asmedigitalcollection.asme.org/article.aspx?articleid=2604111.

---

[2] American Society of Mechanical Engineers has granted permission to post only the paper abstract. A link to the access the paper online is provided above.

3.1 Abstract

Fused Deposition Modeling (FDM) is currently one of the most widely utilized prototyping technologies. Studies employing statistical techniques have been conducted to develop empirical relationships between FDM process factors and output variables such as dimensional accuracy, surface roughness and mechanical properties of the fabricated structures. However, the effects of nozzle Temperature (T), Nozzle-Bed Distance (NBD), and their interactions on Strut Width (SW) have not been investigated. In the present work, a two-way factorial study with 3 levels of T and NBD in triplicates was undertaken. A fixed-effects model with interaction was proposed and remedial measures based on error analysis were performed to obtain correct inferences. The factor main/interaction effects were all found to be statistically significant ($p < 0.05$) using Analysis of Variance (ANOVA). Multiple comparisons were conducted between treatment means using the Tukey's method. A Multiple Linear Regression (MLR) model ($R^2 = 0.95$) was subsequently developed to enable prediction of SW. The developed MLR model was verified experimentally; by 1) the fabrication of individual struts and 2) the fabrication of single-layer scaffolds with parallel raster patterns. The % error between the predicted and observed widths of individually fabricated struts was 3.2%, and the error between predicted and observed SW/spacing for the single-layer scaffolds was ≤5.5%. Results indicate that a similar statistical methodology could be potentially employed to identify levels of T and NBD that yield defined width struts using open architecture, personal or commercial FDM setups and existing/new materials.

Chapter 4

POLY-L-LACTIC ACID: PELLETS TO FIBER TO FUSED FILAMENT FABRICATED

SCAFFOLDS, AND SCAFFOLD WEIGHT LOSS STUDY[3]

Authors: Prashanth Ravi, Panos S. Shiakolas and Tré R. Welch.

Author Contributions: PSS and TRW conceived the research project and designed the study. PR performed the scaffold fabrication and statistical data analysis. TRW recorded weight loss measurements and performed the rheological testing. PR prepared the manuscript which was later critically revised by PSS and TRW.

Link to access the full peer-reviewed and published original research paper: http://www.sciencedirect.com/science/article/pii/S2214860416301385.

---

[3] Used with permission of Elsevier, 2017.

4.1 Abbreviations

CMMB, custom multi-modality 3D bioprinter; PLLA, poly-L-lactic acid; PLA, poly-lactic acid; AM, additive manufacturing; SLS, selective laser sintering; SLA, stereolithography; FFF, fused filament fabrication; 3DP, powder bed and inkjet 3D printing; T_g, glass transition temperature; T_c, crystallization temperature; T_m, melting temperature; VE, viscous extrusion; PP, photo-polymerization; PGA, poly-glycolic acid; PCL, polycaprolactone; PBS, phosphate-buffered saline; LNCS, liquid nitrogen cooling system; DSC, differential scanning calorimetry; L/D, length/diameter; ANOVA, analysis of variance; CAD, computer-aided design; STL, standard tessellation language; RPM, revolution per minute; PID, proportional-integral-derivative; SLA, stereo lithography apparatus; UV, ultra violet; NBD, nozzle-bed distance; PSI, pounds per square inch; SEM, scanning electron microscope.

4.2 Abstract

Poly-l-lactic acid (PLLA) is a bioresorbable polymer used in a variety of biomedical applications. Many 3D printers employ the fused filament fabrication (FFF) approach with the ubiquitous low-cost poly-lactic acid (PLA) fiber. However, use of the FFF approach to fabricate scaffolds with medical grade PLLA polymer remains largely unexplored. In this study, high molecular weight PL-32 pellets were extruded into ~1.7mm diameter PLLA fiber. Melt rheometric data of the PLLA polymer was analyzed and demonstrated pseudo-plastic behavior with a flow index of n=0.465 (<1). Differential scanning calorimetry (DSC) was conducted using samples from the extruded fiber to obtain thermal properties. DSC of the 3D printed struts was also analyzed to assess changes in thermal properties due to FFF. The DSC and rheometric analysis results were subsequently used to define appropriate FFF process parameters. Constant porosity scaffolds were FFF 3D printed

with 4 distinct laydown patterns; 0/90° rectilinear (control), 45/135° rectilinear, Archimedean chords, and honeycomb using the in-house developed custom multi-modality 3D bioprinter (CMMB). The effect of laydown pattern on scaffold bulk erosion (weight loss) was studied by immersion in phosphate-buffered saline (PBS) over a 6-month period and measured monthly. A repeated measures analysis of variance (ANOVA) was performed to identify statistically significant differences between mean percent weight loss of the four laydown patterns at each time point (1-6 months). The resulting data follows distinct temporal trends, but no statistically significant differences between means at individual time points were found. Cross-sectional scanning electron microscope (SEM) images of the 6-month degraded scaffolds showed noticeable structural deterioration. The study demonstrates successful processing of PLLA fiber from PL-32 pellets and FFF-based 3D printing of bioresorbable scaffolds with pre-defined laydown patterns using medical grade PLLA polymer which could prove beneficial in biomedical applications.

KEYWORDS: laydown pattern; scaffold weight loss; poly-L-lactic acid; pellets to fiber processing; fused deposition modeling

4.3 Introduction

In recent years, AM, i.e. 3D printing, is increasingly employed in the biomedical domain for fabricating scaffolds, stents, splints, and other implants. The layer-by-layer or bottom-up fabrication style utilized in 3D printing allows the user to prototype a designed object with intricate features in a relatively short time period without the need to develop part specific tooling or dies. Several 3D printing approaches have been developed and evolved over the past three decades including SLS, SLA, FFF, 3DP, and 3D plotting. The FFF technique 'prints' an object from a CAD model (in .STL file format) by depositing molten plastic in controlled paths generated by a computer slicing program[3]. Additive manufacturing

provides users the ability to customize their design to fulfill desired performance criteria mainly limited by choice of printing technique, material and printing resolution. From a tissue engineering perspective, 3D printing empowers a user to customize scaffold architecture at the design-level while considering performance requirements for the scaffold and fabrication constraints of the printer.

One of the earliest studies investigating the use of PLLA as a biodegradable polymer was reported by Kulkarni et al.[59] in 1971, and one of the first rapid prototyped PLLA structures was reported by Giordano et al.[60] in 1996. Since then, a variety of approaches have been utilized to fabricate structures using PLLA or PLLA copolymerized with other polyesters such as PGA and PCL. These approaches include freeze drying, particulate leaching, phase separation, gas foaming, textile technologies, electrospinning, self-assembly, and inkjet binder based 3D printing[60–68]. Conventional approaches such as freeze drying, salt leaching, phase separation, and electrospinning do not allow for the highly reproducible and controllable fabrication of scaffolds with desired pore structure and interconnectivity[19–23,25]. Moreover, such techniques frequently demand specialized tooling/dies, and often result in structures with poor and unpredictable mechanical properties[24]. Solid freeform fabrication techniques have gained widespread usage owing to their layer-by-layer manufacturing capability and documented reproducibility[25–29,69,70]. Furthermore, scaffolds with intricate structural features can be fabricated due to the layer-by-layer methodology employed. Albeit in the inkjet binder based 3D printing (direct 3DP) of scaffolds, a binder is controllably deposited onto sequential layers of powdered polymer with good reproducibility, there is a limitation of print-head compatibility with organic solvents in addition to the difficulty in removing unbound powder from small/curved channels[71]. Similarly, SLS is more suitable for prototyping metallic structures, and SLA requires the print material to be processed in the form of a liquid resin with appropriate

viscosity. The 3D plotting technique requires the material to have suitable viscoelastic properties in order to be extruded through a nozzle, and subsequently to maintain post-extrusion structural integrity. In the case of inability to process a particular material directly using one of the commonly used techniques, an inverse mold is typically fabricated using a compatible sacrificial material in which the desired material is set. On the other hand, direct fabrication using biocompatible/bioresorbable materials is naturally advantageous since several avoidable parameters are automatically eliminated. FFF offers such an advantage contingent upon the ability to process desired material into fiber with a target diameter and tight tolerance.

Teoh et al. fabricated PCL fibers for scaffold fabrication using FFF, but a similar approach has not been documented in the literature for medical grade PLLA fiber extrusion, or for FFF-based 3D printing of scaffolds using extruded medical grade PLLA fiber[72]. In FFF, polymer fibers melt inside a temperature controlled heated block, commonly referred to as a "hot-end". The molten polymer is forced out of the heated block through a nozzle typically by compressive forces generated using a pinch-roller-motor arrangement, and deposited in computer controlled paths for layer-by-layer fabrication. Even though many 3D printers (commercial and otherwise) employ the FFF approach using commonly available PLA fibers, utilization of FFF to fabricate scaffolds using medical grade PLLA fibers remains largely unexplored. In this research, we hypothesized that FFF could be successfully employed for the rapid fabrication of scaffolds with different laydown patterns using medical grade PLLA polymer. Hutmacher et al. reported that scaffolds FFF 3D printed with different laydown patterns using PCL polymer may be utilized to induce regeneration of multiple tissue types or multiple tissue interfaces[73]. Similarly, Bose et al. have reported that both the biodegradation characteristics and strength degradation

kinetics can be highly influenced by varying parameters such as pore size, geometry, and strut orientation[74].

In this manuscript, we report successful extrusion of PLLA fiber from high molecular weight medical grade PL-32 pellets along with DSC and rheometric polymer data. Extruded fibers were used to characterize the FFF process and the 3D printed struts were analyzed with DSC. The FFF approach was used to fabricate scaffolds with four distinct laydown patterns on the in-house developed CMMB. The scaffold weight loss was studied by immersion in PBS solution for 6 months with weight loss measurements taken monthly. The results of this study show that it is possible to fabricate scaffolds with different laydown patterns using medical grade PLLA and the FFF approach. The results also show that, with additional research, scaffold weight loss could be modulated via FFF-based manufacturing.

4.4 Materials and methods

4.4.1 The CMMB.

The CMMB (Figure 15) used in this research was developed in-house to allow customization of hardware, such as the use of different sized nozzles with each printing modality, independent NBD calibration for individual modules, inclusion of dissimilar printing technologies (FFF, VE, PP), and integration of distinct material types including rigid thermoplastics, viscous polymers and gels/inks[30]. The process parameters on the CMMB are fully defined and controlled by employing open source software tools Repetier-Host (Hot-World GmbH & Co. KG, Willich, Germany) and Slic3r (by Alessandro Ranellucci)[14,31]. One of the FFF modules with a 0.3mm nozzle was used to fabricate the scaffolds analyzed in this study. The CMMB platform has a motion resolution of 3 microns in each of the X, Y, and Z directions.
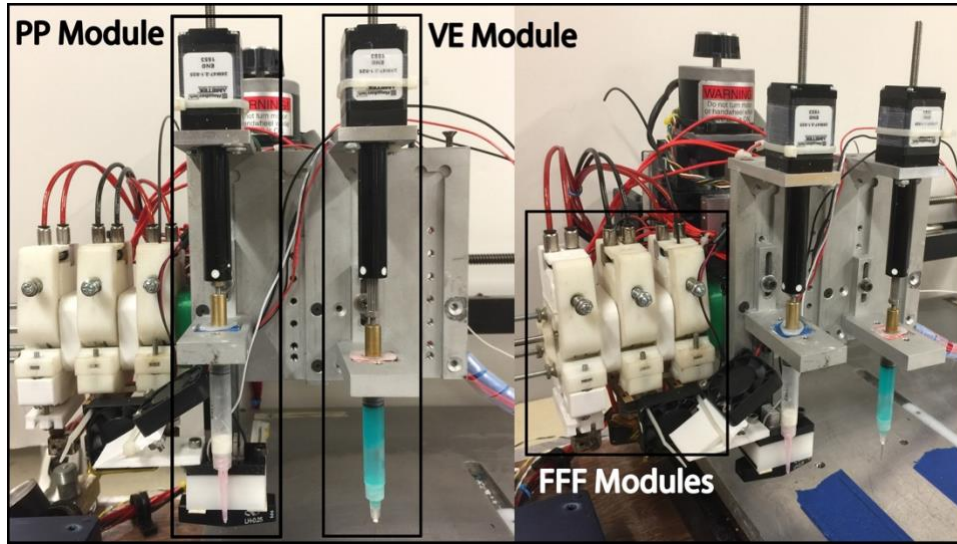
Figure 15. The in-house developed CMMB with the PP, VE, and FFF print modules.

4.4.2 Differential scanning calorimetry (DSC).

Three samples were collected from the extruded PLLA fiber and analysed using a DSC Q20 with LNCS (TA Instruments, New Castle, DE, USA). A temperature heating cycle from 20°C to 220°C at a rate of 10°C/min was applied; then held constant for 1 min, and cooled at 10°C/min. The temperature cycle was repeated and T_g, T_m, T_c, ΔH_m, ΔH_c, and ΔH_{mp} from the second heating cycle were reported. The percent crystallinity was calculated using equation 1. The same procedure was used to analyse 5 samples of 3D printed struts to assess if thermal properties changed because of the FFF process. The fiber was fed into the heated nozzle-block (operating at T=210°C) and extruded struts were collected for DSC.

$$X_c = \frac{\Delta H_m - \Delta H_c}{\Delta H_{mp}} \times 100 \tag{1}$$

where X_c = % crystallinity, ΔH_m = Heat of fusion [J/g], ΔH_c = Heat of crystallization [J/g], and ΔH_{mp} = Heat of fusion for 100% crystalline PLLA = 93.1 J/g[75–77].

4.4.3 PLLA fiber fabrication.

PL-32 granules (Mw=565kDa, PURAC, the Netherlands) were weighed, fed into a hopper, and melt-extruded at 180-185°C ramp profile on a 4-stage melt extruder (ATR-Torque Rheometer, Brabender, Hackensack, NJ, USA) to form cylindrical fibers with a diameter of 1.72±0.3mm.

4.4.4 Rheometry of PLLA fibers.

Three capillary dies, with L/D ratios 15/1, 20/1 and 30/1 were used to determine the viscosity of PLLA upon extrusion. Samples were extruded through the 15/1 and 20/1 dies at extrusion speeds of 1, 5, 10 and 15 RPM for 1 min. Extrusion speeds of 1, 5 and 10 RPM were used with the 30/1 die due to setup limitations. The extruded polymer was collected and weighed (Mettler Toledo XP205, Mettler Toledo LLC, Columbus, OH, USA) for each speed and each capillary die. Polymer viscosity, shear rate and shear stress at each speed of polymer extrusion were obtained using the Winext Viscosity software (Brabender, Hackensack, NJ, USA). The equations for shear rate ($\dot{\gamma}$), shear stress (τ) and apparent viscosity (η) are:

$$\dot{\gamma} = \frac{6 \cdot Q'}{\pi \cdot R^3} \ [1/s] \tag{2}$$

$$\tau = \frac{\Delta p \cdot R}{2 \cdot L} \ [Pa] \tag{3}$$

$$\eta = \frac{\tau}{\dot{\gamma}} \ [Pa \cdot s] \tag{4}$$

where Q' = volumetric flowrate [cm^3/s], R = radius of capillary [cm], Δp = pressure difference [Pa], and L = length of capillary [cm]. The shear stress vs. shear rate (equation 5a) and viscosity vs. shear rate data (equation 5b) were analyzed using the power law relationship[78,79]. The power law equation is a simple mathematical relationship frequently used to model the relationship between shear stress-shear rate and apparent viscosity-shear rate within a limited range of applied shear rates[79].

$$\tau = K\dot{\gamma}^n \tag{5a}$$

$$\eta = K\dot{\gamma}^{n-1} \tag{5b}$$

where K is the consistency parameter and n the flow index.

4.4.5 Experimental design and scaffold CAD model.

Four sets of scaffolds with distinct laydown patterns were fabricated with four replicates per pattern; 1) 0/90° rectilinear, 2) 45/135° rectilinear, 3) Archimedean chords and 4) honeycomb. The 0/90° rectilinear scaffold was used as control in this study. The scaffold geometry (15x15mm^2 square with 5x5x0.5mm^2 corner triangle removed) was modeled in SOLIDWORKS (Dassault Systèmes Americas Corp., Waltham, MA, USA). The thickness was set at 0.8mm, corresponding to four printed layers in the final scaffold.

4.4.6 FFF printing methodology and process parameters.

One of the FFF modules (0.3mm nozzle diameter) on the CMMB was used for scaffold fabrication. The solid model was converted to the .STL file format and imported into the processing software Repetier-Host. The process parameters defined in the slicing software were 0.2mm layer height (and NBD), 600mm/min print-head motion speed, and 210°C nozzle temperature. The extrusion width in the advanced settings of Slic3r was set to 0.3mm (equal to the nozzle diameter). The top surface of the print bed was cleaned using 70% isopropyl alcohol to remove debris. The NBD was checked before every print was initiated to ensure consistent layer height (and NBD) for all the scaffolds. The nozzle temperature was maintained at 210±0.1°C by adjusting the PID controller settings in the printer firmware. The infill density, ratio of build material volume to total scaffold volume, was set at 40% (60% porosity) in the slicing software for all scaffold geometries.

4.4.7 PBS weight loss measurements.

The 3D printed PLLA scaffolds were first weighed dry on a digital scale. Then, they were immersed in a vial containing PBS (GIBCO, Life Technologies, Grand Island, NY, USA) at pH 7.4. The vial was placed on a shaker table in an oven at 37°C operated at 120 RPM. At each time point, the samples were removed, rinsed with distilled water, and dried for 18 hours in a vacuum oven with desiccant before measuring their dry weight. The samples were then re-immersed in fresh PBS solution until the next measurement period. The samples were measured monthly for 6-months. The percent weight loss, ΔX, was calculated using equation 6.

$$\Delta X = \frac{(X_0 - X_i)}{X_0} \times 100 \tag{6}$$

where X_0 and X_i are the initial and i[th] month test dry weights respectively[76].

4.4.8 Scaffold imaging and dimensional accuracy.

The scaffold laydown patterns were imaged using a Nikon Eclipse LV150 digital microscope with 2.5X objective, and NIS Elements software (Nikon Inc., Melville, NY, USA) was used to acquire images and record necessary feature measurements. The full scaffold images were obtained using an 8MP iPhone camera. SEM images were obtained using a Hitachi S-3000N SEM (Hitachi High Technologies America Inc., Schaumburg, IL, USA). The edge-to-edge dimensional accuracy of the printed scaffolds was evaluated in the X-Y plane using calipers.

4.4.9 Statistical analysis.

Average and standard deviation were computed for DSC data and percent scaffold weight loss. A repeated measures ANOVA was performed to check for statistically significant differences ($p < 0.05$) in the mean percent scaffold weight loss between laydown pattern groups at each time point. T-tests were conducted to determine significant differences

(p<0.05) in the thermal properties (T_g, T_m, T_c, %X_c) between extruded PLLA fibers and 3D printed PLLA struts. GraphPad Prism 6 (GraphPad Software Inc., La Jolla, CA, USA) was used for statistical analysis.

4.5 Results

4.5.1 Differential scanning calorimetry (DSC).

The T_g of the extruded PLLA fiber was observed at 62.1±0.3°C, the T_c at 105.6±0.2°C, and the T_m at 176.1±0.4°C. For purposes of melt dispensation systems, the melting temperature is of critical importance, since beyond this temperature the polymer can be extruded through the dispensing nozzle without generating high shear stresses (due to a drop in polymer viscosity). The average percent crystallinity was observed at 22.5±4%. The percentage crystallinity is important as the ordered crystal structure adds further resistance during polymer flow. The average heat of crystallization was 40.4±5.8 J/g and the average heat of melting was 61.4±9.5 J/g. The thermal properties of the extruded PLLA fiber samples are also reported in the Appendix.

The temperature for PLLA fiber extrusion through the 3D printer nozzle was set at T=210°C because it was observed during preliminary experimentation that the PLLA fiber was smoothly extruded at that temperature. The thermal properties of the 3D printed PLLA struts (extruded at T=210°C) are presented in the Appendix (Table 2). T-tests were conducted to compare thermal properties of interest (T_g, T_m, T_c, %X_c) prior to and after the 3D printing process to check for significant differences (p<0.05). The average T_c, T_m, and %X_c of the 3D printed PLLA struts were found to be statistically different (p<0.05) compared to the corresponding properties of the extruded PLLA fiber, respectively. However, the T_g was found not to be significantly different (p>0.05).
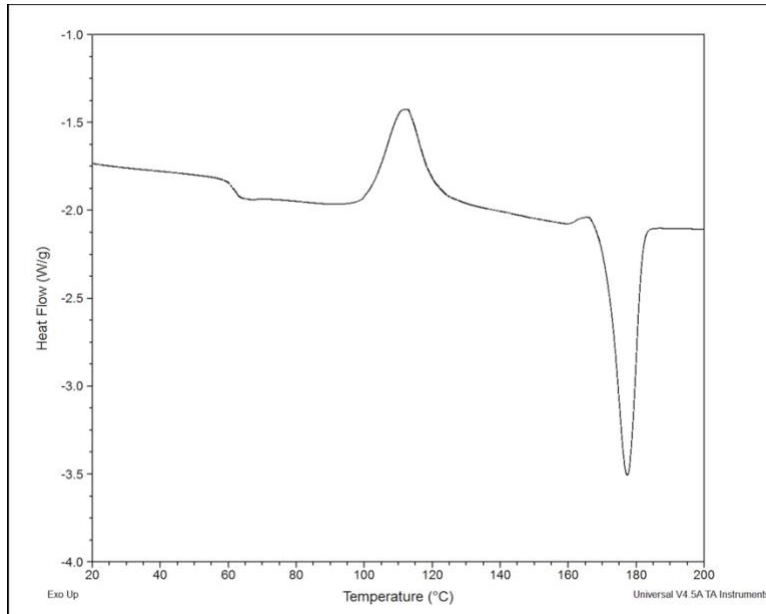
Figure 16. A typical DSC thermal profile of a PLLA polymer sample showing the T_g, T_c, and T_m peaks from left to right, respectively.

4.5.2 Rheological properties of PLLA.

The changes in apparent viscosity, shear stress and shear rate for PLLA obtained using the Brabender Winext Viscosity program are presented in Table 3 in the Appendix section. The apparent viscosity vs. shear rate and shear stress vs. shear rate data were fitted using equations (5a) and (5b), respectively. The obtained value of the consistency parameter (K) was ~25800 and the flow index (n) was 0.465. The apparent viscosity-shear rate and shear stress-shear rate relationships using the power-law curve fit were $\eta = 25800\,\dot{\gamma}^{0.465-1}$ (R^2=0.90) and $\tau = 25756\,\dot{\gamma}^{0.465}$ (R^2=0.88), respectively (Figure 17A/3B).
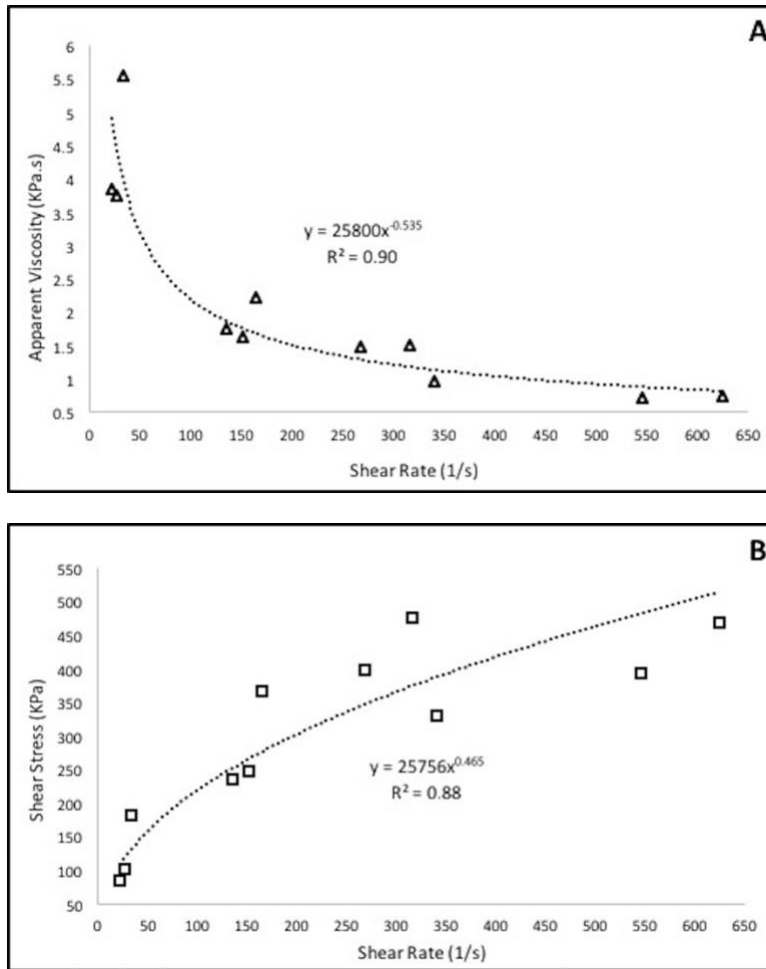
Figure 17. Plots of apparent viscosity vs applied shear rate (A) and shear stress vs applied shear rate (B). Inset power-law fit equations with consistency parameter (K), flow index (n), and corresponding coefficient of determination (R^2).

4.5.3 3D printed scaffolds and percent weight loss.

A representative set of 3D printed scaffolds is presented in Figure 18 with distinct pore designs corresponding to the laydown patterns. For the input STL file i.e. a 15mm x 15mm square with 5mm x 5mm corner triangle removed, the edge to edge dimensional accuracy observed was 15.26±0.14mm x 15.14mm±0.18mm for the 0/90° rectilinear, 15.19±0.04mm x 15.27±0.10mm for the 45/135° rectilinear, 15.23±0.20mm x 15.17±0.27mm for the

Archimedean chords and 15.39±0.12mm x 15.32±0.03mm for the honeycomb scaffolds. Therefore, on average the printed scaffolds were within ~2% of the target 15mm x 15mm designed external geometry. The percent weight loss is plotted as a function of PBS immersion time (in months) for all scaffolds grouped by laydown pattern (Figure 19). No statistically significant differences in the means of the scaffold percent weight loss between different laydown pattern groups were found using ANOVA (p>0.05). However, distinct temporal trends can be observed (Figure 19) in the mean scaffold percent weight loss data. The relatively large standard errors in the percent weight loss data are attributed to the non-uniformity in PLLA fiber diameter (~17% of nominal fiber diameter).
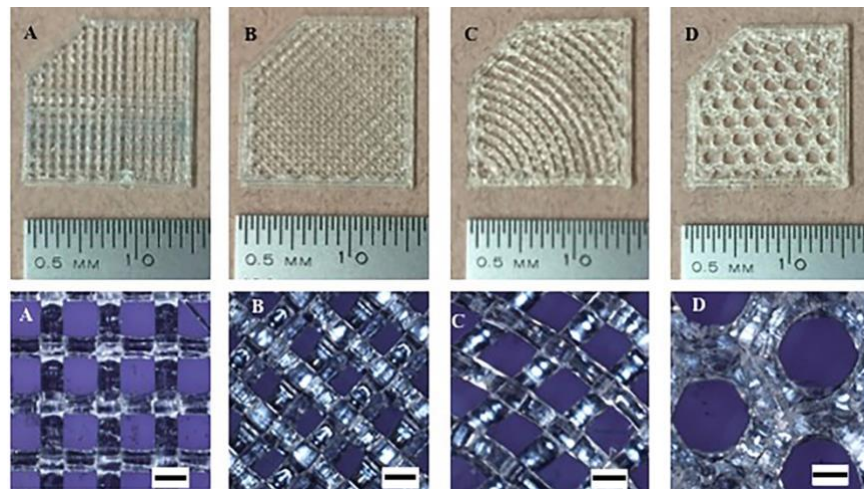
Figure 18. Representative 3D printed scaffolds with 40% fill density (60% porosity) and four laydown patterns for visualization of the overall/porous geometry: (A) 0/90° rectilinear (control), (B) 45/135° rectilinear, (C) Archimedean chords and, (D) honeycomb with corresponding microscopic images of fill patterns. Note: 1 division=0.5 mm for the full scaffold images and the scale bar for the microscopic images=500 microns.
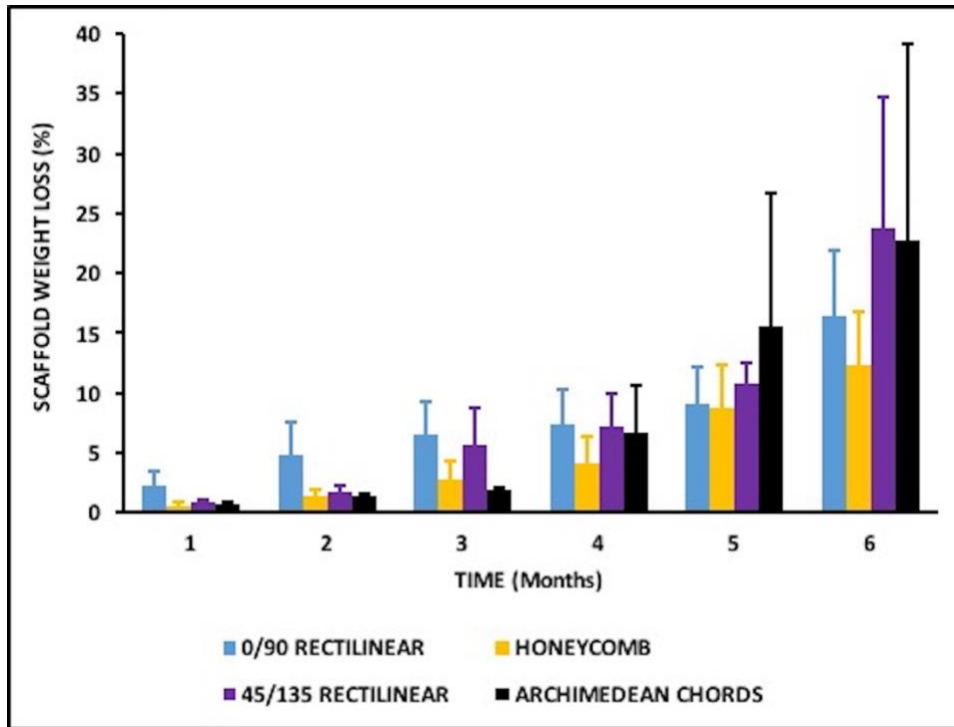
Figure 19. Mean percentage weight loss of the scaffolds as a function of PBS immersion time. Note: Corresponding standard error bars are shown for each laydown pattern type at individual time points.

4.6 Discussion

4.6.1 Rheological/DSC properties and FFF process parameters.

The plot of apparent viscosity vs. shear rate (Figure 17) for PLLA demonstrates non-Newtonian pseudoplastic behavior with flow index *n* less than 1. Apparent viscosity (η) is found to decrease with increasing shear rate (γ̇) indicating a shear-thinning effect, and implying that the PLLA polymer is suitable for extrusion-based processing. The power law curve fit of viscosity-shear rate and shear stress-shear rate data resulted in reasonable values of the coefficient of determination (R^2). The R^2 value for the apparent viscosity-shear rate fit is ~0.90 and for the shear stress-shear rate fit is ~0.88, verifying that the power-law adequately describes much of the observed variability in the apparent viscosity

and shear stress data. From the DSC analysis, the T_m of the extruded fiber was 176.1±0.4°C and of the 3D printed struts was 177.9±0.3°C, both being close to the melt temperature of 178°C reported by Garlotta[80]. Mean percentage crystallinity (%X_c) was calculated at 22.5±4% for the extruded fibers and at 16.3±1.4% for the 3D printed struts (Tables 1 & 2 in the Appendix). The %X_c of the 3D printed struts was found to be significantly lower (p<0.05) than the %X_c of the extruded fibers as a result of rapid quenching due to the high surface area to volume ratio of the small diameter struts, which may have resulted in a higher ratio of the amorphous component[76].

The molecular weight of the medical grade PLLA (M_w=565kDa) used in this study is quite high. Commercial PLA (Shaxon Industries Inc., Anaheim, CA, USA) was observed to be readily extruded at a temperature ~180°C. However, commercial FFF fibers are reported to have an amorphous composition with a range of melting temperatures, and material data are usually not published by the manufacturers[81]. The PLLA used in the present research is a semi-crystalline polymer with a high number of repeating monomer units (M_w=565kDa), and the heavy polymer chains in this PLLA are likely to have provided higher resistance during extrusion through a small orifice. Fang and Hanna have reported that semi-crystalline polymers exhibit greater resistance to flow due to the organized arrangement of molecules within crystal structures, which further enhances the intermolecular forces[79].

The shear stresses generated during extrusion are directly proportional to the polymer viscosity (Equation 4). The apparent viscosity of poly-caprolactone (M_w=20kDa, T_m=57.17°C) as reported by Ramanath et al. during FFF extrusion at 75°C (substantially higher than T_m for PCL at comparable shear rates) varied from ~140Pa s to ~10Pa s from low (~0/s) to high (~450/s) shear rates, respectively[82]. Using the power-law relationship $\eta = 25800\ \dot{\gamma}^{0.465-1}$, the apparent viscosity of PLLA at ~200°C and shear rate ~10.55/s is

estimated to be ~7316 Pa s. It is evident that the apparent viscosity of PLLA is much greater than the apparent viscosity of PCL reported by Ramanath et al. during FFF extrusion, which results in higher resistance to flow during extrusion. As a direct consequence, the force necessary to overcome the required pressure drop for stable flow increases. For smooth extrusion using the pinch-roller based printing arrangement, a reduction in apparent viscosity is essential which is achieved with an increase in the FFF extrusion temperature. Therefore, a higher temperature (T=210°C) was defined for consistent FFF printing of PLLA as it is reported that the apparent viscosity of a polymer decreases as a function of increasing temperature following an Arrhenius relationship, $Ae^{(E/RT)}$, where A is a constant related to melt viscosity, E is the activation energy of viscous flow, R is the universal gas constant and T is the absolute temperature[78,83].

Previous studies with the CMMB revealed that NBD is the most important process parameter influencing strut width compared with nozzle temperature and print head motion speed, within the working range of the controllable parameters[14]. It is common practice in FFF to set the NBD or layer height ~70% of the nozzle diameter for good bonding/adhesion and good mechanical strength of the final 3D printed structure. In this research, the layer height was defined at 0.2mm (~67% of 0.3mm nozzle) in the slicing software. The outflowing molten polymer is reported to be cylindrical in nature with a diameter larger than the diameter of the nozzle orifice due to the die swelling effect[81]. Upon exiting the nozzle, the semi-molten extrudate is "sandwiched" between the traveling nozzle and the print bed or previous layer. The bottom face of the extrudate adheres to the bed (or previous layer) and the top surface is "pressed" by the travelling nozzle generating a partially flat surface on the top of the printed strut, thus providing a robust foundation for the struts of the successive layer. This effect is observable in the SEM image from a previous investigation[14] as well as in Figure 22A/C/E of the current manuscript.

4.6.2 Scaffold weight loss.

The percent weight loss increased with time for all scaffolds irrespective of the laydown pattern type (Figure 19). The 0/90° rectilinear pattern was used as control since it is commonly employed in scaffold fabrication. Chen et al. discussed that scaffold weight loss is affected by the fundamental hydrolysis rate, polymer architecture and matrix size[84]. One of the objectives of the present study was to evaluate weight loss as a function of the scaffold microarchitecture while keeping matrix size and porosity constant. In evaluating the weight loss as a function of microarchitecture, no statistical differences were found using the ANOVA F-tests at each time point. However, distinct temporal trends can be observed (Figure 19) in the mean scaffold percent weight loss data corresponding to different laydown patterns. ANOVA revealed high variability in weight loss within each laydown pattern group analyzed. This variability is attributed to the local dimensional variation of the extruded PLLA fibers (up to ~ 17.7% of the nominal diameter) fabricated using the Brabender extruder. Various struts with widths substantially less or greater than the defined strut width (0.3mm) were observed in fabricated scaffolds (Figure 20) as a result of the non-uniformity in extruded fiber diameter. Strut widths as low as 0.264mm to as high as 0.631mm were observed in some of the scaffolds. This is because the slicing software assumes constant fiber diameter while generating print commands based on defined process parameters. Leong et al. discussed the importance of fiber dimensional uniformity for high accuracy FFF and also found that the build accuracy of constructs may be as low as 0.127/mm[20].

In general, the higher the effective surface area of scaffolds in contact with PBS, the higher the diffusion of water into PLLA and the more the hydrolytic degradation. In the current investigation, the 0/90° and 45/135° patterned scaffolds have nearly identical square pore designs. The Archimedean chords scaffold has a near diamond like pore

shape with curved edges whereas the honeycomb scaffold has a hexagonal pore. However, closer examination of the honeycomb architecture (Figure 18) illustrates how in this case two faces (the bottom/adjacent) of individual struts forming the honeycomb are occluded due to the way in which the honeycomb structures are tightly packed next to each other by the slicing software. Therefore, the surface area effectively available for PBS uptake and thereby bulk erosion is diminished and this is likely why the percent weight loss observed with the honeycomb scaffolds was consistently lower than the other infill patterned scaffolds throughout the 6-month weight loss study. Relatively speaking, the other infill patterned scaffolds are primarily occluded to PBS contact at the interlayer strut-strut bonding points until hydrolytic degradation progresses to a point where debonding between layers occurs.
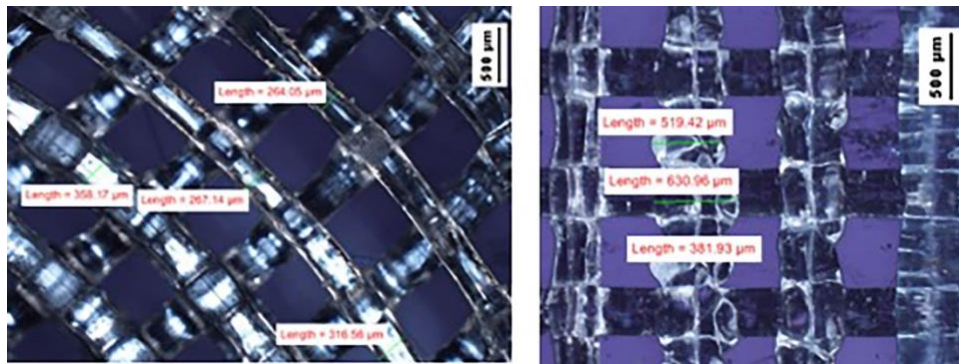
Figure 20. Microscopic images showing inconsistencies in strut widths observed in some of the 3D printed scaffolds due to dimensional variation in the extruded PLLA fiber diameter. Scale bar=500 microns.

PLLA is known to exhibit a swelling effect at the early stages of bulk erosion[85], a behavior that was also observed in the present study (Figure 7). At 6-months of PBS immersion, the samples turned white due to swelling from hydrolysis and bulk weight loss. They were also extremely brittle and prone to fracture during handling due to structural deterioration. Significant cracking/flaking was observed in the scaffolds (Figure 22D-F) due to polymeric degradation, though the observed bulk weight loss was relatively low at the

end of the 6-month immersion period. The highest mean percent weight loss recorded at ~24% for scaffolds with the 45/135° laydown pattern. Layer-layer debonding was also observed (Figure 22A-C) even though struts in the neighboring layers appeared well bonded immediately post-fabrication. The higher exposed surface area per unit volume at the contact points likely resulted in increased PBS contact/infiltration, and possibly a higher rate of polymer erosion. Ratner et al. report that the rate of penetration of PBS into the polymer through the cracks and crevices exceeds the rate of polymer conversion to water-soluble products in bulk erosion, and these cracks and crevices eventually crumble into pieces. The phenomenon explains the brittleness and reduced toughness of the scaffolds that was observed subsequent to the 6-month immersion[86]. The lowering of local pH results in accelerated hydrolysis due to autocatalytic degradation as mentioned by Henton and Rezwan[87,88]. This is further evident when the month to month increase in percent weight loss is evaluated, especially towards the end of the 6-month period, since the hydrolysis of PLLA is a relatively slow process spanning a long time period. Moreover, the bulk erosion mechanism in polymers results in uniform weight loss through the scaffold volume, and is characterized by initially little and subsequently accelerated weight loss (Figure 19), also accompanied by a steady decrease in molecular weight[85]. Such an abrupt increase in the percent weight loss is observable post the 4-month mark with scaffolds belonging to all the four fill patterns. It is also reported that the hydrolysis of polymeric chains tends to occur in the amorphous regions, or at the surface of the crystalline regions in semi-crystalline polymers[86]. The observed mean percent weight loss in the current study was in general lower compared with the weight loss reported in prior studies[89,90]. An average weight loss of ~21% at 6-months (26 weeks) was reported by Gong et al[89], and 13.41% at ~1-month (4 weeks) was reported by Xiong et al.[90]. The differences observed in the percent weight loss between the present investigation and the aforementioned published studies can be

attributed to variations in the experimental methodology. First, the porosity in the current study was set at 60% (40% fill density) for all scaffolds irrespective of the type of laydown pattern, whereas porosity in the cited studies was 60.3% (Xiong et al.)[90] and greater than 94% (Gong et al.)[89]. Second, the molecular weight of PLLA used for scaffold fabrication by Xiong et al. and Gong et al. was 374kDa and 212 kDa, respectively, compared to the substantially higher molecular weight PLLA (565kDa) used in the current research. Makadia et al. have argued that higher molecular weight and crystalline polymers generally exhibit lower weight loss rates[91]. The crystallinity of 3D printed PLLA samples was found to be ~16% from DSC as previously mentioned. Although further research and more data including mechanical properties of the scaffolds is needed to accurately comment on specific applications the scaffolds could cater to, based on observed percent weight loss trends, the honeycomb patterned structures could possibly be employed in applications that require initially slower dissolution rates such as orthopedic fixation devices. On the other hand, the 0/90° rectilinear, 45/135° rectilinear and Archimedean chords patterned scaffolds all showed a near doubling in percent weight loss between the 5-6-month time points, and could possibly be employed in tissue engineering applications requiring relatively faster dissolution rates and/or timed release of drugs or nanoparticles.
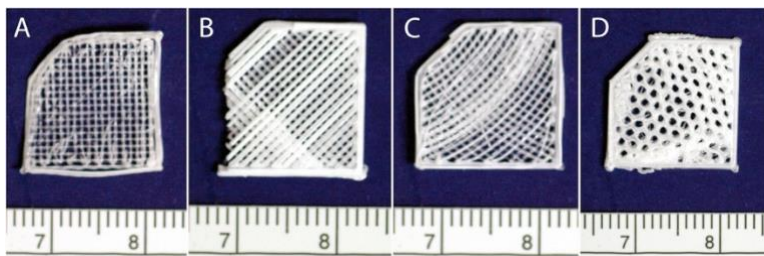
Figure 21. Whiteness due to swelling observed in the scaffolds at 6-months from initial PBS immersion. Scaffolds with (A) 0/90° rectilinear (control), (B) 45/135° rectilinear, (C) Archimedean chords and, (D) honeycomb patterns. Scale 1 division=1mm.

52
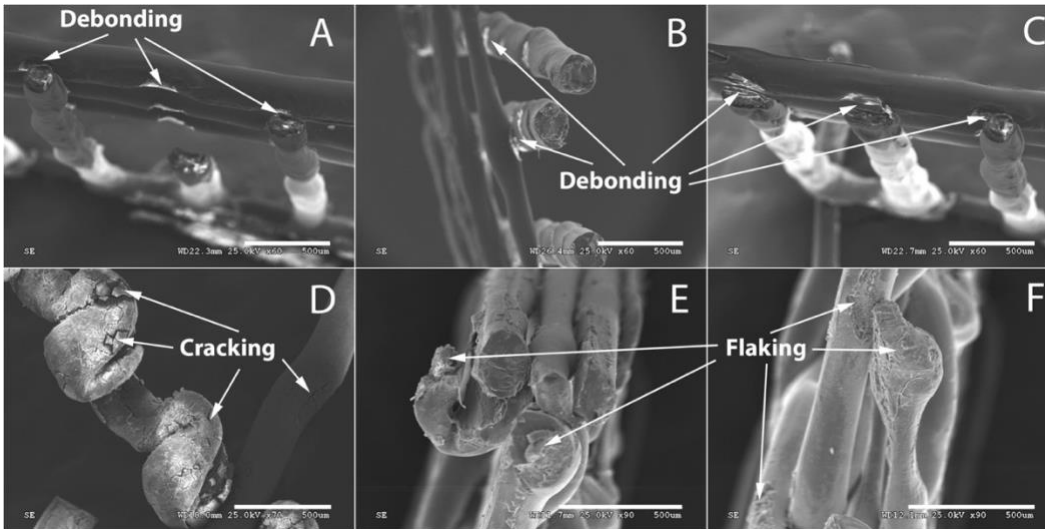
Figure 22. SEM images of scaffolds after 6 months of PBS immersion showing layer-layer debonding (A-C), and cracking/flaking (D-F) due to polymer degradation and bulk erosion. Note: Some unevenness in strut geometry due to variation in PLLA fiber diameter is observable in the D & F images. Scale bar=500 microns.

4.7 Conclusions

In this study, PLLA fiber was successfully extruded from high molecular weight medical grade PL-32 pellets. Rheometric data of the PLLA fiber showed pseudoplastic behavior with the flow index n=0.465 (<1) and consistency parameter K~25800. DSC data of the extruded PLLA fibers and the 3D printed struts were analyzed and showed statistically significant differences in certain thermal properties. Results from the DSC and rheometric analysis were used to define appropriate FFF process parameters for scaffold fabrication using PLLA. The extruded fiber was used to 3D print constant porosity scaffolds with four distinct laydown patterns using an in-house developed 3D printer. The dry weight of the printed scaffolds was measured at one-month time points for six months during PBS immersion to evaluate the effect of laydown pattern on percent weight loss. Although dissimilar temporal trends in the percent weight loss data are visible as a function of PBS immersion time for different laydown patterns, no statistically significant differences in the

mean percent weight loss between different laydown groups at each time point were found. Structural deterioration including cracking/flaking and layer-layer debonding were observed in the 6-month degraded scaffolds. The maximum observed percent weight loss for the scaffolds at the end of the 6-month PBS immersion period had a mean of ~24%. It is postulated that with further research, it may be possible to fabricate bioresorbable PLLA scaffolds with modulated weight response for tissue engineering applications such as bone implants or controlled drug/nanoparticle using FFF.

4.8 Acknowledgements

4.9 Appendix A

Table 1. Thermal properties of the extruded PLLA fibers from DSC.

Sample	T_g (°C)	T_m (°C)	ΔH_m (J/g)	T_c (°C)	ΔH_c (J/g)	%X_c
1	61.9	175.7	51.9	105.6	34.7	18.5
2	62.5	176.4	70.8	105.7	46.2	26.4
3	61.9	176.3	61.4	105.4	40.3	22.7
Average ± SD	62.1±0.3	176.1±0.4	61.4±9.5	105.6±0.2	40.4±5.8	22.5±4.0

Table 2. Thermal properties of the 3D printed PLLA struts from DSC.

Sample	T_g(°C)	T_m(°C)	ΔH_m(J/g)	T_c(°C)	ΔH_c(J/g)	%X_c
1	62.2	177.4	60.0	112.6	43.4	17.8
2	61.1	177.8	47.0	112.7	33.5	14.5
3	61.1	178.2	46.6	111.6	32.5	15.1
4	62.3	178.2	45.2	111.8	29.6	16.7
5	62.3	178.1	45.4	111.9	29.3	17.2
Avg±SD	61.8±0.6	177.9±0.3	48.8±6.3	112.1±0.5	33.7±5.7	16.3±1.4

Table 3. Rheometric data of the PLLA polymer obtained using the Brabender setup.

No	L/D	Speed [RPM]	T [°C]	Δp [psi]	$\dot{m}$ [g/min]	$\dot{V}$ [cm³/min]	$\dot{\gamma}$ [1/s]	τ [KPa]	η [Pa.s]
1	15/1	1	200.0	1589	0.24	0.19	32.9	182.6	5555.0
2	15/1	5	199.8	3185	1.21	0.97	164.3	366.0	2226.9
3	15/1	10	199.7	4142	2.32	1.86	315.1	476.0	1510.6
4	15/1	15	199.9	4080	4.60	3.68	624.7	468.9	750.5
5	20/1	1	202.3	1184	0.20	0.16	27.3	102.0	3738.0
6	20/1	5	202.4	2869	1.11	0.89	150.8	247.2	1640.1
7	20/1	10	200.2	3843	2.50	2.00	339.5	331.2	975.5
8	20/1	15	199.4	4571	4.01	3.21	544.6	393.9	723.3
9	30/1	1	201.7	1492	0.16	0.13	22.3	85.7	3848.6
10	30/1	5	200.6	4085	0.99	0.79	134.5	234.7	1745.7
11	30/1	10	199.8	6919	1.97	1.58	267.6	397.6	1485.9

4.10 Appendix B (unpublished data)

The following storage modulus and T_g data was not part of the published research article. The T_g for the 3D printed PLLA scaffolds (~66°C) was slighlty higher than the T_g for the raw PLLA polymer (~62°C) as seen in Figure 23 and Figure 24. The scaffolds with

Honeycomb fill pattern demonstrated the highest storage modulus (~4.2GPa), which makes sense given the symmetrical vertical stacking of the rasters which drastically increases the layer-layer contact area compared to the other hatched fill patterns which have fewer layer-layer contact area. However, high variability was oberved in the storage modulus values for the Archimedean chords and 0/90 rectilinear fill patterned scaffolds (Table 4), which is again attributed to the relatively high variation in the PLLA fiber diameter employed to 3D print the scaffolds.
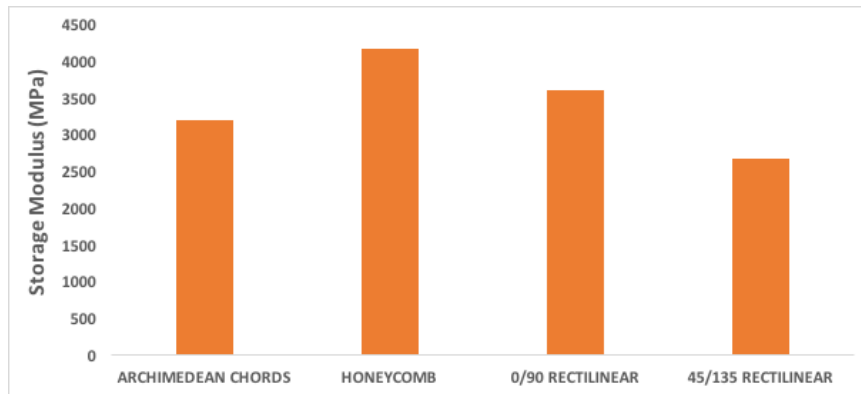
Figure 23. Bar graph showing average storage modulus values versus infill pattern groups.
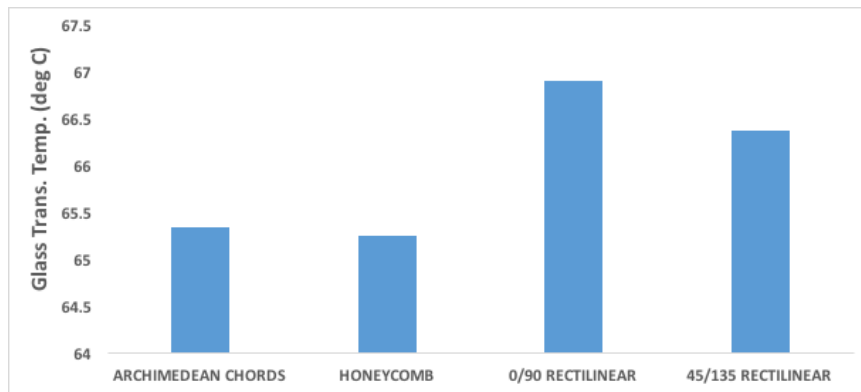
Figure 24. Bar graph showing average T_g values versus infill pattern groups.

Table 4. Average ± SD for storage modulus and T_g values versus infill pattern.

Infill Pattern	Storage Modulus (MPa)	Tg (℃)
ARCHIMEDEAN CHORDS (n=3)	3208 ± 1372	65.3 ± 0.9

HONEYCOMB (n=3)	4178 ± 119	65.3 ± 2.5
0/90 RECTILINEAR (n=3)	3606 ± 1655	66.9 ± 0.3
45/135 RECTILINEAR (n=3)	2675 ± 285	66.4 ± 1.1

Chapter 5

3D PRINTING OF POLY (GLYCEROL SEBACATE FUMARATE) GADODIAMIDE-POLY

(ETHYLENE GLYCOL) DIACRYLATE STRUCTURES AND CHARACTERIZATION OF

MECHANICAL PROPERTIES FOR SOFT TISSUE APPLICATIONS[4]

Authors: Prashanth Ravi, Jamie Wright, Panos S. Shiakolas and Tré R. Welch.

Author Contributions: PR, PSS and TRW conceived the project and designed the study. PR 3D printed the samples, recorded sample weights and performed the statistical data analysis. DMA testing was performed by PR and JW. PR prepared the manuscript which was later critically revised by PSS, TRW and JW.

---

[4] The version in this chapter is the submitted (pre-peer review) version used with permission from John Wiley & Sons, 2017.

5.1 Abstract

Bioresorbable materials have been frequently used to 3D print biomedical structures. In this study, we developed a technique to 3D print poly (glycerol sebacate fumarate) gadodiamide (Rylar)-poly (ethylene glycol) diacrylate (PEGDA) samples and investigated their mechanical and thermal properties as a function of print speed (PS) and ultra-violet intensity (UVI). The Young's modulus (E), ultimate tensile strength (UTS), failure strain (ε_F), and glass transition temperature (T_g) showed strong correlation with PS and UVI. Results showed E to be between 1.31-3.12MPa, UTS between 0.07-0.43MPa and ε_F between 7-20% with brittle failure. The T_g was observed to lie between -54.48℃ to -49.10℃ without secondary/tertiary transitions. Dominant elastic behavior was observed from the Dynamic Mechanical Testing (DMA) viscoelastic data. Testing results were used to develop a regression predictive model for E as a function of PS and UVI. The model performance was evaluated experimentally with an average absolute error of 3.62%. The E and stress-strain response of our 3D printed samples show agreement with published data for human tracheal cartilage, and the mechanical properties were similar to other published soft polymeric scaffolds/patches. The E´ moduli were also similar to bovine articular cartilage. We have successfully demonstrated that Rylar, a novel bioresorbable radiopaque polymer, when blended with PEGDA can be 3D printed controllably for soft tissue applications such as airway obstructions.

KEYWORDS: 3D printing, Rylar, photopolymerization, bioresorbable radiopaque polymer, tracheomalacia

59

5.2 Introduction

Although bioresorbable materials have long been explored for their functionality in providing structural support and/or aiding tissue regeneration, only relatively recently have such materials been used with 3D printing technologies for medical applications[15,60,73]. Additive Manufacturing (AM) techniques enable the fabrication of complex geometries and structures with customized features without the necessity for part-specific dies or molds[92]. A variety of approaches including Fused Deposition Modeling (FDM), Powder Bed and Inkjet 3D Printing (3DP), Selective Laser Sintering (SLS), Stereo Lithography Apparatus (SLA) and 3D Plotting have been used by researchers to fabricate medical structures[5,71].

Materials including metals, natural and synthetic polymers, ceramics and composites have been explored for hard and soft tissue applications. Soft materials have been explored primarily in the context of cardiovascular research. Langer et al. investigated a new polymer poly (glycerol-sebacate) to fabricate cardiovascular patches for use in repairing heart defects[93]. GoreTex has long been used in adults for arterial vessel grafting and in pediatric fontan procedures[94]. He et al. employed inkjet 3D printing and a novel ink composed of polycaprolactone dimethylacrylate (PCLDMA) mixed with PEGDA, although their technique involved significant UV post curing in addition to the in situ photopolymerization[95].

One potential use of 3D printing is for treating tracheomalacia resulting from congenital heart disease[96]. Tracheomalacia is characterized by a collapse of the airway due to overt softening of the cartilage[97]. Research groups in the past have investigated the fabrication of airway splints and/or stents using materials such as polycaprolactone (PCL), Marlex mesh stiffened with silastic cement or nitinol[98–102]. Stents have had higher successes in general due to their less invasive nature compared to splinting, although granulation tissue formation is a common concern[103]. Freitag et al. found that

epithelialization altered the dynamic properties of naked metal stents which limited their feasibility in tracheomalacia[104]. Vinograd et al. successfully 3D printed silastic Marlex mesh splints without major complications[98]. Zopf et al. 3D printed a splint using PCL with no unexpected issues after a year of surgery and full splint resorption anticipated in three years[101]. Morrison et al. successfully 3D printed personalized PCL devices for 3 young patients with life threatening tracheobronchomalacia and achieved promising results[105]. However, the long-term effects of tissue integration, infections and erosion of splints into neighboring structures from these investigations are unknown[106,107].

In the current research, our aim was to investigate the 3D printing of a novel radiopaque polymer, Rylar, mixed with PEGDA as a candidate material for treating soft tissue complications such as tracheomalacia. We used a customized 3D printer and developed a fabrication methodology by combining controlled in situ photopolymerization and extrusion 3D printing[31,108]. The 3D printed structures were characterized for their mechanical and thermal properties using Dynamic Mechanical Analysis (DMA) as a function of controlled process parameters PS and UVI. The obtained mechanical and thermal properties were compared to published properties of human tracheal tissue, other human/animal soft tissues and biomaterial structures to evaluate feasibility for application to tracheomalacia or other soft tissue ailments.

5.3 Materials and methods

5.3.1 Rylar Synthesis and Material Preparation

Rylar was synthesized as previously published by a transesterification reaction to a molecular weight $M_w = 6000$ Da[108–110]. PEGDA ($M_w = 575$ Da, Sigma Aldrich) was mixed in 50% wt/wt with Rylar to serve as a biocompatible crosslinking agent.

5.3.2 In-house 3D Printing Setup and Methodology

The open architecture Custom Multi-Modality 3D Bioprinter (CMMB) used in the current research was developed in-house to enable hardware customization and the ability to fabricate structures using multiple materials either standalone or in combination[14,30]. The CMMB can be used to fabricate structures using thermoplastic, viscous polymeric and colloidal materials employing filament and Direct Ink Writing (DIW) based 3D printing techniques. The photopolymerization (PP) module used in the current research was developed using a Bluewave 75 UV lamp (Dymax Corporation, Torrington, CT) which can irradiate with 9+W/cm^2 in the UVA (320-395nm) wavelength range. An Accu-Cal 50 radiometer (Dymax Corporation, Torrington, CT) was used to monitor and set the intensity prior to each run. The radiometer has a spectral sensitivity centered at 365nm and a resolution of ±1mW/cm^2. A 4mmx3mmx2mm UV hat (Figure 25) was designed around the syringe tip to prevent crosslinking inside the needle and clogging during fabrication. The energy dosages measured using the radiometer were 424mJ/cm^2, 578mJ/cm^2, 289mJ/cm^2 and 400mJ/cm^2 for treatments 1-4 respectively, during a single pass across the 9mm diameter sensor. In the current research, two process parameters, UVI and PS were investigated. The levels were set at 175mW/cm^2 and 250mW/cm^2 for UVI, and 400mm/min and 600mm/min for PS (Table 5).
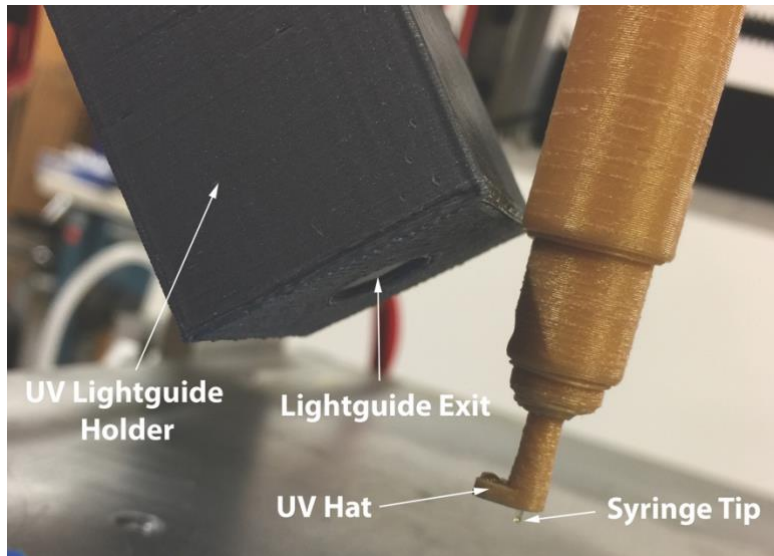
Figure 25. View of the PP module showing the UV blocker hat. The lightguide to syringe tip distance is maintained at 37mm and the lightguide angle is fixed at 40° to the syringe.

Table 5. Design of Experiments setup with treatments and corresponding process parameter levels. Each treatment was fabricated in triplicates (n=3).

Treatment number	PS [mm/min]	UVI [mW/cm^2]
1 (n=3)	400	175
2 (n=3)	400	250
3 (n=3)	600	175
4 (n=3)	600	250

A rectangular solid 40mmx5mmx0.8mm, corresponding to four 0.2mm thick printed layers, was modeled and converted to the Standard Tessellation Language (STL) file format using SolidWorks (SolidWorks Corp., Waltham, MA). The model was sliced using Slic3r/Repetier-Host (Hot-World GmbH & Co. KG, Germany). The G-codes were modified to print all 4 layers with an orientation along the 40mm sample length (Figure 26). The UV lamp was on throughout the fabrication of each sample at the appropriate intensity.

An in-house designed and 3D printed fixture was used to mount the UV lightguide at a 40°

angle to the syringe and a normal distance of 37mm away from the tip. A fifth scanning

layer without material being dispensed but with identical parameters was included to UV

scan the printed sample and ensure adequate crosslinking. The scanning layer was

executed at a Z-height of 1.8mm. The infill density was set at 75%, layer height at 0.2mm

(4 printed layers), and extrusion width at 0.25mm. 3cc syringes (Global Medical, Port St.

Lucie, FL) with a 0.25mm translucent PTFE tip (Weller, Apex, NC) were used to dispense

the resin. After printing, the samples were removed, air dried and weighed using a Sartorius

precision balance (Precision Weighing Balances, Bradford, MA).
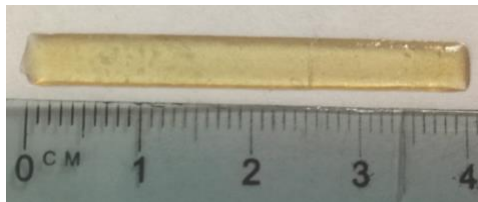
Figure 26. A representative 40mmx5mmx0.8mm 3D printed Rylar-PEGDA sample. Scale: 1 division=1mm.

5.3.3 Mechanical Properties

A RSA G2 DMA machine (TA Instruments, New Castle, DE) was used for testing. For static

tensile testing a loading gap of 10mm, linear rate of 0.08mm/sec and preload of 0.05N

were applied. DMA was used to evaluate the viscoelastic properties of the polymer. A

frequency sweep was performed at a room temperature of ~23°C using a loading gap of

10mm, preload of 0.2N, 0.15% strain and frequency of 0.1-10Hz to stay within the linear

viscoelastic region. The properties of the 3D printed specimens including the E, UTS, ε_F,

the storage modulus (E´) and loss modulus (E´´) were evaluated based on results from the

static and dynamic tensile tests. The E was calculated from the linear region of the true

stress vs. true strain curve[111].

5.3.4 Thermal Properties

Tests were performed using a temperature sweep at a rate of 3°C/min applied over a temperature range of -60 to 40°C. The strain was 0.15% at a frequency of 1Hz and a loading gap of 10mm. The T_g was found from the peak of the E´´ curve according to the ASTM D 4065-2001 standard.

5.3.5 Statistical and Regression Analysis

ANOVA was performed on the treatment groups for the mechanical/thermal properties followed by a Bonferroni post-hoc test performed on Young's modulus with a null hypothesis being no significant difference ($p < 0.05$) in the treatment means (n=3 per group). Testing data were used in a regression analysis to develop a predictive model for polymer stiffness as a function of process parameters UVI and PS. A Box Cox transformation with $\lambda = 3$ was applied to ensure normally distributed and uncorrelated residuals. The performance of the model was evaluated by fabricating samples at 4 arbitrary combinations of UVI and PS (Table 6). Statistical software used was Minitab 17 (Minitab Inc., State College, PA, USA).

Table 6. Setting codes with corresponding process parameters levels to evaluate the performance of the regression model used for predicting E. The PS and UVI process parameter levels were randomly selected. Two samples were fabricated at each setting (n=2).

Setting code	PS [mm/min]	UVI [mW/cm^2]
I (n=2)	550	200
II (n=2)	500	225
III (n=2)	450	190
IV (n=2)	475	215

5.4 Results

5.4.1 Sample Weights

Average sample weights for the experimental treatments (1-4) are highly consistent with most samples weighing between 125-130mg (Table 7). The standard deviations are within 5% of the average sample weight demonstrating a consistent fabrication process.

Table 7. Weights for the experimental treatments (1-4) and settings codes (I-IV). Data reported are mean ± std. dev. Sample size provided in parentheses next to the treatment/setting code.

Treatment or setting code	PS [mm/min]	UVI [mW/cm^2]	Weight (mg)
1 (n=9)	400	175	127.9±2.0
2 (n=9)	400	250	127.5±2.6
3 (n=9)	600	175	122.8±0.7
4 (n=9)	600	250	127.5±1.7
I (n=2)	550	200	130.9±6.0
II (n=2)	500	225	130.5±1.9
III (n=2)	450	190	130.6±0.4
IV (n=2)	475	215	132.0±4.2

5.4.2 Mechanical Properties

The mechanical properties of the printed samples are listed in Table 9. The analysis showed that holding the UVI constant and increasing PS resulted in reduced E, UTS and ε_F. At a constant UVI of 175mW/cm^2 while increasing the PS resulted in a 53% reduction in E. Similarly, a UVI of 250mW/cm^2 showed a 32% reduction in E with increasing PS. The UTS at a UVI of 175mW/cm^2 showed an 83% reduction and a 37% reduction at a UVI of

250mW/cm^2 when PS increased. Similarly, the ε_F of the printed samples showed a reduction with increasing PS at constant UVI with a 65% reduction in strain at 175mW/cm^2 and a 5% reduction in ε_F at 250mW/cm^2. The ε_F at a constant UVI of 175mW/cm^2 showed a reduction of 65% and at 250mW/cm^2 a reduction of 5%. ANOVA showed significant differences between the treatment means for the E, UTS and ε_F data. Analyzing the E at the UVI of 175mW/cm^2 and 250 mW/cm^2 showed a statistical difference between a PS of 400mm/min and 600mm/min, and a statistical difference was found between the UVI of 175mW/cm^2 and 250mW/cm^2 at a PS of 600mm/min using the Bonferroni post hoc test. Overall, increasing the PS results in a lower E, whereas a higher UVI resulted in a printed specimen with higher E. The engineering stress-strain curve showed a linear relationship between applied stress and strain as shown in Figure 28 which was immediately succeeded by brittle failure without any yielding.

The UVI is a measure of the number of incident photons per unit time per unit area (intensity), and PS determines the total number of photons incident at a unit area (dosage). It was observed that E is correlated with energy dosage (mJ/cm^2) per pass as shown in Table 8. The highest energy dosage (treatment 2) yielded the highest E, followed by treatments 1, 4 and 3, which demonstrated decreasing E corresponding to the decreasing energy dosage. From the Bonferroni comparisons, all treatment pairs except 1 and 2 are significantly different at 95% confidence. This suggests that at lower PS, which corresponds to higher exposure time, the effect of intensity level on E becomes less critical. Such behavior is expected since the degree of conversion initially increases rapidly, but later plateaus with increasing exposure time resulting in diminishing returns with further increases in energy dosage due to the logarithmic nature of the relationship[112]. The plot in Figure 27 of average E for each of the 4 treatments vs. single pass energy dosage confirms the logarithmic nature of the relationship (R^2=0.90), and is further corroborated by

comparing the ratio of E for treatments 2 and 1 (1.12) with the ratio of dosage for treatments 2 and 1 (1.36). Although the exposure energy increase by 36% from treatment 1 to 2, the E increased only by 12%. However, the effect of intensity level was more pronounced at higher PS (corresponding to lower exposure time), and a comparison of E for treatments 4 and 3 (higher PS) shows that E increased by 63% for a corresponding 38% increase in energy dosage due to increase in UVI, which supports the assessment that UVI has more effect at lower exposure times.
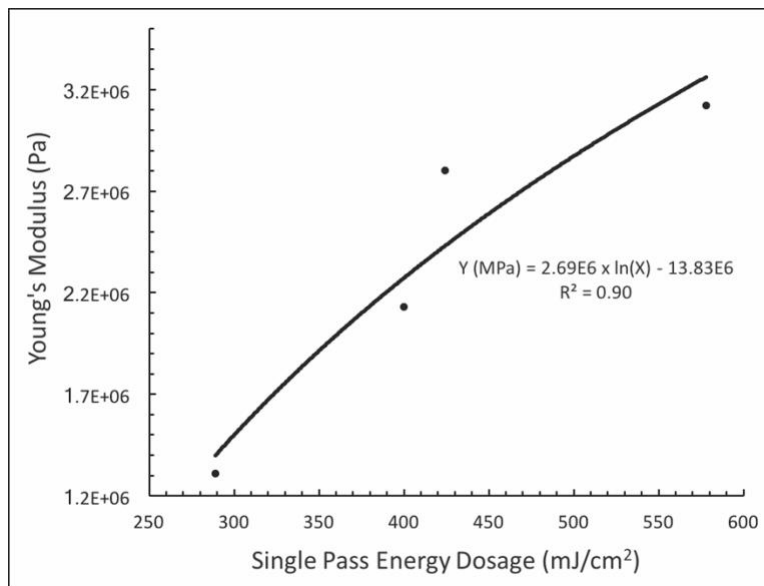
Figure 27. Average E for the 4 treatment groups vs. single pass energy dosage showing good logarithmic fit (R^2=0.90).
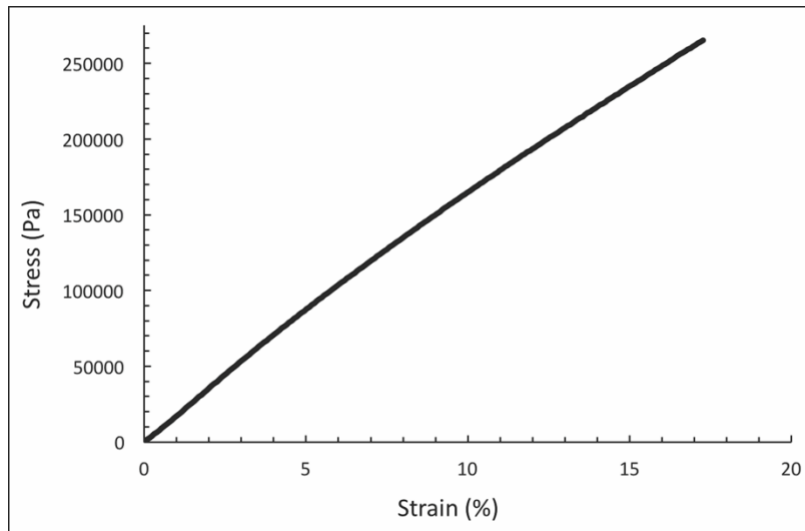
Figure 28. A typical engineering stress-strain curve from tensile testing of a Rylar-PEGDA sample.
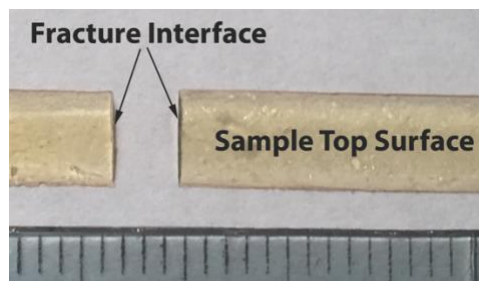
Figure 29. Representative image of a tested sample showing sample top and fracture interface. Scale: 1 division=1mm.

Table 8. Treatment number, average E values, and single pass energy dosages across the radiometer sensor at the respective treatments.

Treatment number	PS [mm/min]	UVI [mW/cm^2]	E [MPa]	UTS [MPa]	Fail Strain [%]
1 (n=3)	400	175	2.80 ± 0.05	0.42 ± 0.04	20 ± 1
2 (n=3)	400	250	3.12 ± 0.06	0.43 ± 0.06	17 ± 3
3 (n=3)	600	175	1.31 ± 0.01	0.07 ± 0.02	7 ± 2
4 (n=3)	600	250	2.13 ± 0.02	0.27 ± 0.08	16 ± 4

A typical stress-strain curve for the static tensile tests is presented in Figure 28. After a small initial toe region, the crosslinked polymer showed linear elastic deformation right to the point of sample failure. The fracture occurred abruptly having a sharp surface without any necking or other distortion, which is typical of brittle failure (Figure 29). After the initial unkinking of molecular chains at low strain (toe region), the sample undergoes linear deformation with respect to applied extensional stress followed by a final rupture of covalent bonds. The UTS was positively related to UVI and negatively related to PS as observed from the average UTS values in . The UTS data closely follows what was observed with E and reaffirms that the effect of UVI on UTS reduces at lower PS (longer exposure time). ε_F followed a trend similar to what was observed with the E and UTS data.

Table 9: Mechanical properties from the 3D printed specimens, data reported as mean ± std dev.

Treatment number	E [MPa]	Energy dosage per pass across the radiometer sensor [mJ/cm^2]
1	2.80	424
2	3.12	578
3	1.31	289
4	2.13	400

5.4.3 Dynamic mechanical analysis (DMA)

DMA testing provides insight into the viscoelastic properties of the 3D printed samples. It was found that E´ was quite stable within the testing region (0.1-10Hz) with very little noticeable change, whereas E´´ experienced a dip with increasing frequency (Figure 30).

70
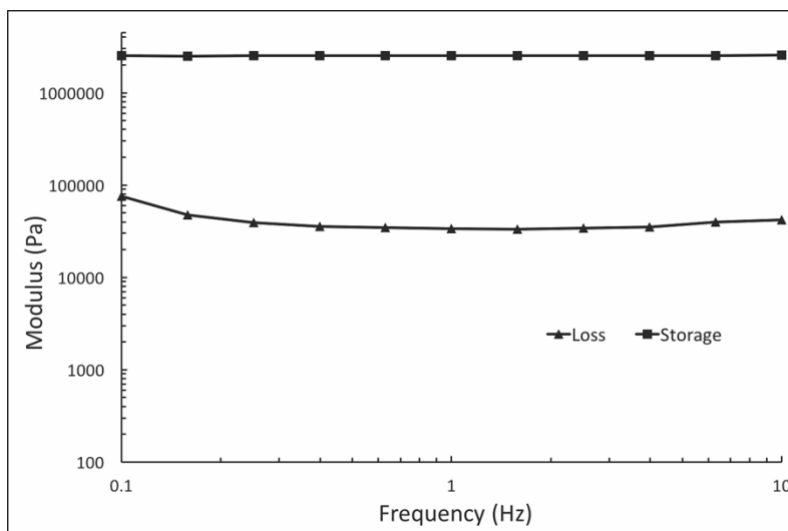
Figure 30. Representative E´ and E´´ data for treatment 1 from the frequency sweep testing.

From the frequency sweep data plot (Figure 30), the E´´ was ~40 times lower than E´ values, which demonstrates a dominant elastic response stemming from a high degree of crosslinking. The E´´ shows a small dip with increasing frequency which is expected since higher frequency oscillations do not provide the sample enough time to relax and respond by dissipating energy via molecular rearrangements.

5.4.4 Glass transition temperature

An increase in T_g was observed with increasing UVI at constant PS, whereas T_g decreased with increasing PS at constant UVI (Table 10). No secondary transition was observed within the -60 to +40°C temperature range from Figure 31, and the E´´ showed a distinct peak which was used to evaluate the T_g. The E´ was stable above -15°C up to +40°C. ANOVA showed significant differences between all T_g treatment means.

Table 10. Average T_g found from the E´´ peaks. Data reported as mean ± SD, n=3 per treatment group.

Treatment number	PS [mm/min]	UVI [mW/cm^2]	T_g [°C]
1 (n=3)	400	175	-50.78±0.54
2 (n=3)	400	250	-49.10±1.13
3 (n=3)	600	175	-54.48±0.06
4 (n=3)	600	250	-52.80±0.65

The T_g range was observed between -55°C (onset temperature) to -30°C (endset temperature) for most samples. Furthermore, no gamma or beta transitions are observed and the rubbery plateau (>15°C) of the E´´ curve was consistent up to 40°C with no melting, which is typical of thermoset polymers because of retained chemical crosslinks. The absence of gamma or beta transitions indicates a high degree of crosslinking.

5.4.5 Regression model

Regression analysis was performed to obtain the relationship between UVI and PS given in parametric form in Equation 1 (λ = 3). The parameter estimates for PS, UVI and the constant (intercept) term in the equation are all statistically significant (p<0.05). E was negatively affected by PS and positively by UVI. The high R^2 (98.23%) is an indication of the goodness of the regression model which explains most of the observed variability in the E dataset.

$$E = \sqrt[\lambda]{\lambda * 2219093^{\lambda-1}(2972590 - 6834\,PS + 7238\,UVI) + 1} \qquad \text{Equation 1}$$
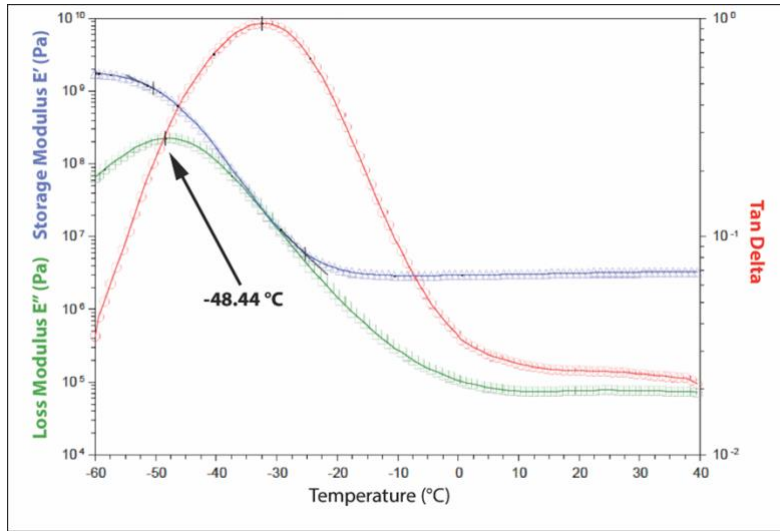
Figure 31. A representative plot of the temperature ramp test from -60 to +40℃ with E´ (blue), E´´ (green) and tan delta (red). The E´´ curve peak is used to evaluate T_g in accordance with the ASTM D 4065-2001 standard.

A total of 4 settings (I-IV) with random combinations of PS and UVI were chosen and 2 samples were fabricated at each setting for tensile testing. The regression model from Equation 1 was used to predict E based on the arbitrarily selected PS and UVI levels. The observed E using setting III (Figure 31) does not have an associated standard deviation because one sample failed abruptly during testing. It was also observed from the process parameter coefficients in Equation 2 that E was slightly more sensitive to changes in UVI compared to PS. The percentage error was calculated using Equation 2. As observed in

Table 11, the highest absolute error was 7.05% with an average absolute error of 3.62%.

$$\% \ error = \frac{(observed - predicted)}{predicted} \times 100\% \qquad \qquad \text{Equation 2}$$

73

Table 11. Predicted vs. observed E (Pa) with corresponding percentage errors.

Setting code	PS [mm/min]	UVI [mW/cm^2]	Predicted E [MPa]	Observed E [MPa]	Percent error
I (n=2)	550	200	2.14	2.16 ± 0.03	0.85
II (n=2)	500	225	2.60	2.48 ± 0.16	-4.35
III (n=1)	450	190	2.66	2.60*	-2.25
IV (n=2)	475	215	2.67	2.48 ± 0.05	-7.05

* Note that standard deviation is unavailable at this setting since one sample failed abruptly during testing.

5.5 Discussion

In this research, we investigated the applicability of 3D printed Rylar-PEGDA as a candidate material for treating soft tissue conditions such as tracheomalacia. We studied mechanical and thermal properties of 3D printed Rylar samples and found the polymer's stiffness to be between 1.31-3.12MPa, UTS to be between 0.07-0.43MPa, ε_F to be between 7-20%, and T_g to be between -54.48℃ to -49.10℃ based on the 4 selected treatment levels. The mechanical properties of our 3D printed scaffolds were comparable with properties of similar soft polymers. The mechanical properties of Rylar – PEGDA 3D samples were similar to poly glycerol sebacate (PGS)[93]. Rylar-PEGDA's stiffness was on average higher than that of molded PGS. The mechanical properties of PGS patches ranged in stiffness from 0.056-1.2MPa, in fail strain from 41-448% and in UTS from 0.23-0.47MPa[113]. Kemppainen et al. reported the tangent modulus of 3D printed PGS scaffolds at 10% strain to be 0.57MPa, that is a lower stiffness in comparison to our 3D printed samples[114]. In a study by Guan et al. the UTS and fail strain of solvent extracted poly (ester urethane) urea

scaffolds are higher, 0.97-1.64MPa and 214-294%, respectively, compared to our results[115]. In another study by Zein et al. the compressive stiffness and yield strength of 3D printed PCL scaffolds ranged between 4 to 77MPa, which is higher than the tensile stiffness of our samples[23].

In comparison to PEGDA structures, Chan et al. 3D printed 20% wt PEGDA structures with compressive stiffness of 503kPa that is weaker than Rylar. Mazzoccoli et al. reported a compressive stiffness of 400kPa for molded disks composed of 20 wt% mixture of 20/80 M_w 3400/400 PEGDA[116,117]. The addition of PEGDA to Rylar as a crosslinking agent allowed for photopolymerization and yielded lower Young modulus values compared to the thermally cross-linked Rylar of 4.4 MPa as reported by Welch et al[108]. Furthermore, Cvetkovic et al. found that 3D printed PEGDA specimens in tension increased with increased energy dosage (Figure 27 and

Table 8), similar to our experimental results[112].

Ito et al. studied the viscoelastic properties of pig airway smooth muscle cells from 0.12-3.5Hz and found the E'' to increase from 10-45KPa, which is lower than what we observed, although we noticed a decrease in E'' (70-50KPa from 0.1-10Hz) with increasing frequency[118]. However, their applied strain (10%) is much higher compared to the 0.15% strain we applied for DMA, and their E' increased from 80-100KPa compared to E' from our experiments which are much higher (~2MPa) with no noticeable change with increasing frequency of oscillation. Moroni et al. found that the E' of bovine articular cartilage increased from about 1MPa to 10MPa between 0.1-10Hz similar to our results; however, our E' was stable with increasing frequency[119]. The T_g for PEGDA (M_w = 575Da) was found to be -31℃ in a study by Keim et al. which is higher than the T_g for our 3D printed PEGDA – Rylar samples, with the shift most likely attributed to the presence of Rylar[120].

A study by Rains et al. found that the Young's modulus for human tracheal tissue ranged between 1-15MPa depending on the age of the individual with the stiffness progressively increasing from inside to outside layers[121]. Roberts et al. reported average Young's modulus for human tracheal cartilage ranging between 4.6-13.6MPa from middle zone to the albumenal superficial zone with a linear stress-strain response up to 10% strain[122]. The Young's modulus for Rylar-PEGDA specimens in our research averaged from 1.31-3.12MPa with the stress-strain response observed to be linear up to 15% strain on average. This indicates agreement in property with the native tissue and suggests applicability of 3D printed Rylar-PEGDA towards splint and/or stent fabrication for tracheomalacia. Moreover, because we observed strong positive correlation between the energy dosage and polymer stiffness (see Figure 27), we anticipate being able to achieve higher polymer stiffness by further increasing the incident UV intensity and/or exposure time (by reducing print speed).

3D printing techniques have been demonstrated to enable the highly reproducible and customized fabrication of complex structures with the ability to achieve desired features unavailable with traditional techniques such as freeze drying, salt leaching, electrospinning and phase separation[19,20,123]. Such high reproducibility primarily stems from the robust control that 3D printing techniques provide over fabrication process parameters. The good reproducibility of our 3D printing methodology is evident by the consistency of the Rylar-PEGDA sample weights, and mechanical and thermal properties within treatment groups. By controllably varying UVI and PS we observed consistent and predictable changes in mechanical and thermal properties, E, UTS, ε_F and T_g. The low layer thickness (0.2mm) in combination with the high-energy dosages in our 3D printing methodology ensured a high level of photocrosslinking as observed by the dominance of

the elastic component from viscoelastic data as well as the robust E from tensile stress-strain data.

The regression model in Equation 2 successfully enabled the prediction of polymer stiffness for 3D printed Rylar-PEGDA as verified using 4 random combinations of PS and UVI. An average absolute error of 3.62% was found between predicted and experimental values for the 4 PS/UVI combinations. Most 3D printing approaches for fabricating biomaterial scaffolds or devices rely primarily on changing the material distribution within the scaffold matrix (at the design or tool path planning stage) in order to customize scaffold mechanical properties to meet functional requirements[39]. Kemppainen et al. discussed the desirability of being able to alter the material modulus as opposed to matrix porosity dictated by tissue growth requirements[114]. However, the ability to tailor the Young's modulus by being able to define and control fabrication process parameters such as PS and UVI when combined with the customized distribution of material within a structural matrix may enable the design of implants with improved functional properties even when conflicting performance criteria such as high porosity (void fraction) and high structural strength are required.

In this study, the primary motivation was the development of a 3D printing methodology to investigate the effects of process parameters on the mechanical and thermal properties of Rylar-PEGDA, a bioresorbable radiopaque polymer for tracheomalacia, a soft tissue application. The ability to modulate the stiffness of the Rylar-PEGDA polymer, as demonstrated in this research, could be employed in the fabrication of customized implantable devices by allowing the definition of desired Young's modulus at the design stage. The control on Young's modulus could prove beneficial for patient-specific implant fabrication for tracheomalacia or other similar soft tissue applications.

5.6 Conclusions

In this research, we developed a technique based on controlled in-situ photopolymerization coordinated with syringe extrusion to successfully 3D print with Rylar, a radiopaque bioresorbable polymer, mixed with PEGDA, a crosslinking agent. Overall, it is observed that both process parameters PS and UVI strongly affect the mechanical and thermal properties of the 3D printed samples as demonstrated by ANOVA and/or post-hoc testing. The performance of a developed regression model for predicting Young's modulus is evaluated by 3D printing samples using random combinations of PS and UVI and found to accurately predict Young's modulus with less than 5% average error. The mechanical properties of the 3D printed structures showed agreement with the properties of human tracheal tissue and published data for other soft polymers, and the viscoelastic properties showed agreement with bovine cartilage while revealing an elastic response suggestive of good photoinitiated crosslinking. In summary, we have successfully demonstrated that the developed methodology and process can be used to 3D print Rylar-PEGDA structures with reproducible and modulated properties for treating soft tissue conditions such as tracheomalacia.

5.7 Appendix A: PLLA-Rylar-PEGDA composite structures (unpublished data)

It was found that the Young's modulus of photocured Rylar-PEGDA was in the lower spectrum of the Young's moduli for human tracheal tissue. To improve the mechanical properties, the incorporation of PLLA was hypothesized. The present discussion reports on the preliminary fabrication of thin PLLA-Rylar-PEGDA disks as a first step towards the fabrication of a composite tubular structure to be employed as splint for treating tracheomalacia. The disks are currently under fabrication and will be evaluated for their overall compression modulus/strength and PLLA to Rylar-PEGDA bond strength. The

process parameters of interest is the speed used to print the Rylar-PEGDA layer which will determine the bond strength based on the corresponding UV exposure time.

A hollow disk with 10mm outer diameter, 6mm inner diameter and 0.8mm thickness was modeled using SolidWorks (Dassault Systèmes Americas Corp., Waltham, MA, USA). The 0.4mm thick base was fabricated with PLLA using a 0.4mm FFF head. The parameters used were 100% fill density, concentric infill pattern and 0.2mm layer height. The PLLA base was printed at a constant 600mm/min for all samples. Rylar-PEGDA was printed on top of the 0.4mm PLLA base. The thickness was again set at 0.4mm (2 layers) with 80% infill, concentric infill pattern, 0.2mm layer height and 0.25mm extrusion width. A 0.25mm PTFE was used to dispense Rylar-PEGDA.
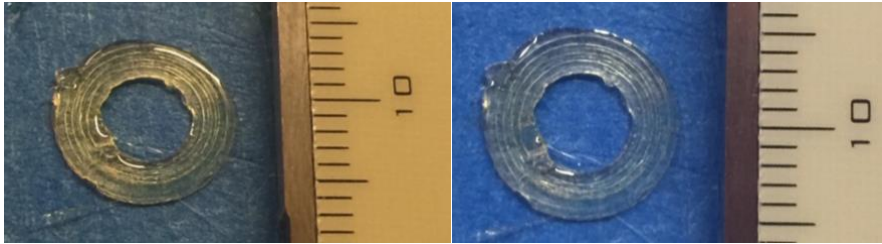
Figure 32. PLLA-Rylar-PEGDA composite disks, top view on the right shows concentric PLLA rasters and angled view on the left shows photocured Rylar-PEGDA bonded with PLLA. The disk is 10mm OD and 6mm ID with 0.4mm PLLA base (2 layers) and 0.4mm Rylar-PEGDA (2 layers) on top. Scale: 1 division=1mm.

Chapter 6

SUMMARY, CONCLUSIONS AND RECOMMENDATIONS FOR FUTURE RESEARCH

The dissertation began by introducing the fundamentals of additive manufacturing as well as the scope and context of the research in Chapter 1. The development of an open architecture 3D printer was discussed at length in Chapter 2 (Aim 1), specifically the hardware development and firware modification aspects. The methodology to process G-codes for fabricating single/multi material structures was discussed along with potential applications. Open source software was used to control the printer in an effort to aid reproducibility of findings discussed in this research. In Chapter 3 (Aim 2), a Design of Experiments study was conducted to study the relationship between raster width and the nozzle-bed distance and nozzle temperature process parameters. Strong correlation was observed between the controlled process parameters and raster width. The nozzle-bed distance was found to be the more dominant of the two parameters investigated. A predictive model was developed for raster width as a function of the two process parameters using regression analysis, and was experimentally verified. It was postulated that such models could be employable in fabricating scaffolds with improved dimensional accuracy of pore sizes, raster widths and porosities for tissue engineering applications. Chapter 4 (Aim 3) discussed the 3D printing and weight loss response of medical grade PLLA scaffolds fabricated with 4 distinct infill patterns. Rheological properties of the PLLA were assessed and showed pseudoplastic behavior. No significant differences in weight loss were observed between scaffolds with different infill patterns. There was large variability in the weight loss data which was attributed to the relatively high variability in the PLLA fiber diameter which was used as feedstock for 3D printing. However, based on the weight loss trends observed, such PLLA scaffolds could be employable in applications where controlled and timed degradation is desired.

In Chapter 5 (Aim 3), the printability of a newly developed biocompatible bioresorbable photocurable resin (Rylar-PEGDA) was discussed. Subsequently, the Rylar-PEGDA resin was used to 3D print coupons that were tested for their mechanical and thermal properties as a function of controlled process parameters UV intensity and print speed. Strong correlation was observed between the properties and process parameters with the print speed having a more dominant effect on the analyzed properties based on ANOVA. A predictive model was developed for the Young's modulus of the resin as a function of the process parameters and was successfully verified experimentally. The mechanical properties showed agreement with properties of human tracheal tissue as well as published data for other soft polymeric patches and scaffolds indicating suitability for use as material for fabricating splints/stents for tracheomalacia. Finally, a composite PLLA and Rylar-PEGDA disk was fabricated (Aim 4) and preliminary observations were reported (Appendix of Chapter 5). The composite disk lays the foundation for fabricating a hybrid reinforced tubular splint for treating tracheomalacia. A major conclusion from the dissertation research is the successful fabrication of structures using novel bioresorbable materials and extrusion-based 3D printing technologies. Some of the structures were 3D printed with customized properties which further reaffirms the versatility of extrusion AM approaches towards manufacturing tailored constructs.

Recommendations for Aim 1: One recommendation for future work is to evaluate a pneumatic syringe extrusion modality in conjunction with the current linear actuator (stepper motor) based piston extrusion. The stepper motor control offers precision in terms of the volume of liquid dispensed, but has a lag in the extrusion start/stop control. The pneumatic setup will offer instantaneous start/stop if there is a pressure controller interfaced with the 3D printer process control card, although a real-time control of pressure will be essential to ensure precision in the volume of liquid dispensed depending on the

apparent viscosity (shear rate) and amount of liquid inside the syringe. Another recommendation is to provide improved support for multiple modalities in the firmware. Currently the firmware supports only one feeder motor at a time and an M92 command must be used to change the axis_steps_per_mm prior to switching between feeder motors. Furthermore, reserving distinct labels for FFF module engagement (P0, P1, etc.) and the extruder motors (T0, T1, etc.) is beneficial but increases the post-processing of G-codes substantially. Thus an alternative approach to achieve both simultaneously must be sought. Finally, a better method to calibrate the X-Y-Z offsets between modules is necessary. An optical (laser) or electrical (limit switch) calibration system can be helpful in accurately calibrating the Z-positioning of each modality.

Recommendations for Aim 2: A recommendation is to study the relationship between raster geometry (width and height) and controlled process parameters for subsequent layers i.e. from layer 2 onwards. This is because the first layer is in contact with the substrate (print bed) whereas the subsequent layers are in contact with rasters from preceding layers thus presenting disparate substrates for the extruded polymer in the glassy state. Moreover, the raster geometry for subsequent layers (layer 2 onwards) is also dependent on the porosity which results in a bridging effect between adjacent rasters from the preceding layer. Finally, the effect of print speed could also be studied (in addition to temperature and nozzle-bed distance) to capture the impact of polymer residency time (inside the hotend) as well as the time of proximity to the print location on raster geometry.

Recommendations for Aim 3: A recommendation is to investigate the mechanical and viscoelastic response of the material and fabricated scaffolds using static/dynamic mechanical testing to gain further insight into the material capabilities and potential applications in the biomedical domain. Comparing the weight loss of the porous scaffolds with a dense (100% fill) scaffold would provide better insight into the relationship between

effective surface area and weight loss. In addition, evaluating the static/dynamic compressive properties of the scaffolds will provide more appropriate information on the applicability of scaffolds to hard tissue applications such as bone tissue engineering.

In the second part of the aim, the effect of UV intensity and the print speed process parameters on the mechanical and thermal properties of Rylar was successfully investigated. A recommendation for the work is to investigate the compressive properties of the 3D printed constructs to complement data from pure tensile testing. This data would provide more insight into the behavior of the material and potential usages. Another recommendation is to increase the viscosity of Rylar so that it is extruded as "filament" rather than forming a droplet at the nozzle in an effort to enhance the structural integrity of printed constructs. Finally, adding a biocompatible photoinitiator and acrylate to Rylar itself could eliminate the need to mix in PEGDA, which was the biocompatible crosslinking agent employed in the current study. If appropriately modified, Rylar could be potentially employable as a resin with SLA 3D printing technology to fabricate tall structures such as a 10-20mm tall splint for tracheomalacia without being restricted by viscous effects that dominate in extrusion 3D printing.

Recommendations for Aim 4: One issue is the geometry of the UV hat designed around the needle of the PP module in order to prevent clogging inside the tip during fabrication. In certain instances the hat occludes significant amounts of UV radiation such as when fabricating smaller geometries, and a hat with a smaller footprint is essential to enable higher UV intensities and exposure times around the needle. Once the fabrication of bi-layered PLLA and Rylar-PEGDA disks is established, the future step would be to 3D print a tall tubular structure with alternating PLLA and Rylar-PEGDA layers as a stepping stone towards a composite tracheal splint with improved characteristics. A significant challenge here would be gaging the impact of printing high temperature PLLA (200+℃) on

photocrosslinked Rylar-PEGDA in addition to the adhesion between the two disparate layers (PLLA and Rylar-PEGDA). The effects of printing high temperature PLLA on crosslinked Rylar-PEGDA as well as adhesion between the 2 layers should be investigated systematically in order to evaluate feasibility of fabricating tall hybrid PLLA/Rylar-PEGDA splints for tracheomalacia.

References

(1) Office, A. M. Additive Manufacturing : Pursuing the Promise. *Energy Effic. Renew. Energy* **2012**.

(2) Hull, C. W. Apparatus for Production of Three-dimensional Objects By Stereolithography, 1986.

(3) Crump, S. S. Apparatus and Method for Creating Three-Dimensional Objects, 1992.

(4) Cesarano III, J.; Segalman, R.; Calvert, P. Robocasting provides moldless fabrication from slurry deposition. *Ceram. Ind. VO - 148* **1998**, *148* (4), 94.

(5) Murphy, S. V; Atala, A. 3D bioprinting of tissues and organs. *Nat. Biotechnol.* **2014**, *32* (8), 773–785.

(6) Lam, C.; Mo, X.; Teoh, S.; Hutmacher, D. Scaffold development using 3D printing with a starch-based polymer. *Mater. Sci. …* **2002**, *20* (1–2), 49–56.

(7) Williams, J. M.; Adewunmi, A.; Schek, R. M.; Flanagan, C. L.; Krebsbach, P. H.; Feinberg, S. E.; Hollister, S. J.; Das, S. Bone tissue engineering using polycaprolactone scaffolds fabricated via selective laser sintering. *Biomaterials* **2005**, *26* (23), 4817–4827 DOI: 10.1016/j.biomaterials.2004.11.057.

(8) Tumbleston, J. R.; Shirvanyants, D.; Ermoshkin, N.; Janusziewicz, R.; Johnson, A. R.; Kelly, D.; Chen, K.; Pinschmidt, R.; Rolland, J. P.; Ermoshkin, A.; et al. Continuous liquid interface production of 3D objects. *Science (80-.).* **2015**, *347* (6228), 1349–1352.

(9) Bose, S.; Roy, M.; Bandyopadhyay, A. Recent advances in bone tissue engineering scaffolds. *Trends Biotechnol.* **2012**, *30* (10), 546–554 DOI: 10.1016/j.tibtech.2012.07.005.

(10) Kalita, S. J.; Bose, S.; Hosick, H. L.; Bandyopadhyay, A. Development of controlled porosity polymer-ceramic composite scaffolds via fused deposition modeling. *Mater. Sci. Eng. C* **2003**, *23* (5), 611–620 DOI: 10.1016/S0928-4931(03)00052-3.

(11) Lee, J.; Choi, B.; Wu, B.; Lee, M. Customized biomimetic scaffolds created by indirect three-dimensional printing for tissue engineering. *Biofabrication* **2013**, *5* (4), 45003 DOI: 10.1088/1758-5082/5/4/045003.

(12) Sood, A. K.; Ohdar, R. K.; Mahapatra, S. S. Parametric appraisal of mechanical property of fused deposition modelling processed parts. *Mater. Des.* **2010**, *31* (1), 287–295 DOI: 10.1016/j.matdes.2009.06.016.

(13) Lee, B. H.; Abdullah, J.; Khan, Z. A. Optimization of rapid prototyping parameters for production of flexible ABS object. *J. Mater. Process. Technol.* **2005**, *169* (1), 54–61 DOI: 10.1016/j.jmatprotec.2005.02.259.

(14) Ravi, P.; Shiakolas, P. S.; Thorat, A. D. Analyzing the Effects of Temperature, Nozzle-Bed Distance, and Their Interactions on the Width of Fused Deposition Modeled Struts Using Statistical Techniques Toward Precision Scaffold Fabrication. *J. Manuf. Sci. Eng.* **2017**, *139* (7), 1–9.

(15) Ravi, P.; Shiakolas, P. S.; Welch, T. R. Poly- l -lactic Acid: Pellets to Fiber to Fused Filament Fabricated Scaffolds, and Scaffold Weight Loss Study. *Addit. Manuf.* **2017**, *16*, 167–176.

(16) Ravi, P.; Wright, J.; Shiakolas, P. S.; Welch, T. R. 3D printing of poly (glycerol sebacate fumarate) gadodiamide-poly (ethylene glycol) diacrylate structures and characterization of mechanical properties for soft tissue applications (in review). *J. Biomed. Mater. Res. Part B*.

(17) Ravi, P. Four-wheel variable counter steering, University of Texas at Arlington,

2013.

(18)   Ravi, P. Development of a modular 3D bioprinter for fabricating tailorable
         biomedical implants using a combination of Inkjet, Viscous Extrusion and Fused
         Filament Fabrication print technologies. In *The 11th Annual Celebration of
         Excellence by Students (ACES)*; University of Texas at Arlington: Arlington, TX,
         2015.

(19)   Hutmacher, D. Scaffold design and fabrication technologies for engineering
         tissues—state of the art and future perspectives. *J. Biomater. Sci. Polym. Ed.*
         2001, *12* (1), 107–124.

(20)   Leong, K.; Cheah, C.; Chua, C. Solid freeform fabrication of three-dimensional
         scaffolds for engineering replacement tissues and organs. *Biomaterials* **2003**, *24*
         (13), 2363–2378.

(21)   Xu, T.; Zhao, W.; Zhu, J.; Albanna, M.; Yoo, J.; Atala, A. Complex heterogeneous
         tissue constructs containing multiple cell types prepared by inkjet printing
         technology. *Biomaterials* **2013**, *34* (1), 130–139 DOI:
         10.1016/j.biomaterials.2012.09.035.

(22)   Luo, Y.; Wu, C.; Lode, A.; Gelinsky, M. Hierarchical mesoporous bioactive
         glass/alginate composite scaffolds fabricated by three-dimensional plotting for
         bone tissue engineering. *Biofabrication* **2013**, *5* (1), 15005 DOI: 10.1088/1758-
         5082/5/1/015005.

(23)   Zein, I.; Hutmacher, D. W.; Tan, K. C.; Teoh, S. H. Fused deposition modeling of
         novel scaffold architectures for tissue engineering applications. *Biomaterials* **2002**,
         23 (4), 1169–1185.

(24)   Russias, J.; Saiz, E.; Deville, S.; Gryn, K.; Liu, G.; Nalla, R. K.; Tomsia, A. P.
         Fabrication and in vitro characterization of three-dimensional organic/inorganic
         scaffolds by robocasting. *J. Biomed. Mater. Res. Part A* **2007**, *83* (2), 434–445
         DOI: 10.1002/jbm.a.

(25)   Lee, K.-W. K.; Wang, S.; Lu, L.; Jabbari, E.; Currier, B. L.; Yaszemski, M. J.
         Fabrication and characterization of poly (propylene fumarate) scaffolds with
         controlled pore structures using 3-dimensional printing and injection molding.
         Tissue Eng. **2006**, *12* (10), 2801–2811 DOI: 10.1089/ten.2006.12.ft-222.

(26)   Castilho, M.; Dias, M.; Gbureck, U. Fabrication of computationally designed
         scaffolds by low temperature 3D printing. *Biofabrication* **2013**, *66* (3), 911–917
         DOI: doi:10.1088/1758-5082/5/3/035012.

(27)   Shim, J.; Lee, J.; Kim, J.; Cho, D. Bioprinting of a mechanically enhanced three-
         dimensional dual cell-laden construct for osteochondral tissue engineering using a
         multi-head tissue/organ building. *J. Micromechanics Microengineering* **2012**, *22*
         (8), 85014 DOI: 10.1088/0960-1317/22/8/085014.

(28)   Khalil, S.; Nam, J.; Sun, W. Multi-nozzle deposition for construction of 3D
         biopolymer tissue scaffolds. *Rapid Prototyp. J.* **2005**, *11* (1), 9–17 DOI:
         10.1108/13552540510573347.

(29)   Derby, B. Printing and prototyping of tissues and scaffolds. *Science* **2012**, *338*
         (6109), 921–926 DOI: 10.1126/science.1226340.

(30)   Ravi, P.; Shiakolas, P. S.; Welch, T. R.; Saini, T.; Guleserian, K. J.; Batra, A. On
         the Capabilities of a Multi-modality 3D Bioprinter for Customized Biomedical
         Devices. In *Proceedings of the ASME 2015 International Mechanical Engineering
         Congress and Exposition*; ASME: Houston, Texas, 2015; pp 1–7.

(31)   Ravi, P.; Shiakolas, P. S.; Oberg, J. C.; Faizee, S.; Batra, A. On the Development
         of a Modular 3D Bioprinter for Research in Biomedical Device Fabrication. In
         Proceedings of the ASME 2015 International Mechanical Engineering Congress

and Exposition; ASME: Houston, Texas, 2015; pp 1–8.

(32) Mohamed, O. a.; Masood, S. H.; Bhowmik, J. L. Optimization of fused deposition modeling process parameters: a review of current research and future prospects. *Advances in Manufacturing*. 2015, pp 42–53.

(33) Peng, A.; Xiao, X.; Yue, R. Process parameter optimization for fused deposition modeling using response surface methodology combined with fuzzy inference system. *Int. J. Adv. Manuf. Technol.* **2014**, *73*, 87–100 DOI: 10.1007/s00170-014-5796-5.

(34) Mohamed, O. A.; Masood, S. H.; Bhowmik, J. L. Optimization of fused deposition modeling process parameters for dimensional accuracy using I-optimality criterion. *Measurement* **2016**, *81*, 174–196 DOI: 10.1016/j.measurement.2015.12.011.

(35) Wang, C. C.; Lin, T.-W.; Hu, S.-S. Optimizing the rapid prototyping process by integrating the Taguchi method with the Gray relational analysis. *Rapid Prototyp. J.* **2007**, *13* (5), 304–315 DOI: 10.1108/13552540710824814.

(36) Rayegani, F.; Onwubolu, G. C. Fused deposition modelling (fdm) process parameter prediction and optimization using group method for data handling (gmdh) and differential evolution (de). *Int. J. Adv. Manuf. Technol.* **2014**, *73* (1–4), 509–519 DOI: 10.1007/s00170-014-5835-2.

(37) Montero, M.; Roundy, S.; Odell, D. Material characterization of fused deposition modeling (FDM) ABS by designed experiments. *Proc. Rapid …* **2001**, 1–21.

(38) Sun, Q.; Rizvi, G. M.; Bellehumeur, C. T.; Gu, P. Effect of processing conditions on the bonding quality of FDM polymer filaments. *Rapid Prototyp. J.* **2008**, *14* (2), 72–80 DOI: 10.1108/13552540810862028.

(39) Hollister, S. J. Porous scaffold design for tissue engineering. *Nat. Mater.* **2005**, *4* (7), 518–524.

(40) Lin, C. Y.; Kikuchi, N.; Hollister, S. J. A novel method for biomaterial scaffold internal architecture design to match bone elastic properties with desired porosity. *J. Biomech.* **2004**, *37* (5), 623–636 DOI: 10.1016/j.jbiomech.2003.09.029.

(41) Ravi, P.; Shiakolas, P. S.; Thorat, A. D. Analyzing the Effects of Temperature, Nozzle-bed Distance and their Interactions on the Width of Fused Deposition Modeled Struts using Statistical Techniques Towards Precision Scaffold Fabrication. *ASME J. Manuf. Sci. Eng.*

(42) Yamaguchi, S.; Ueno, A.; Akiyama, Y.; Morishima, K. Cell patterning through inkjet printing of one cell per droplet. *Biofabrication* **2012**, *66* (3), 911–917.

(43) Xu, T.; Jin, J.; Gregory, C.; Hickman, J. J.; Boland, T. Inkjet printing of viable mammalian cells. *Biomaterials* **2005**, *26* (1), 93–99 DOI: 10.1016/j.biomaterials.2004.04.011.

(44) Xu, C.; Zhang, M.; Huang, Y.; Ogale, A.; Fu, J.; Markwald, R. R. Study of Droplet Formation Process during Drop-on-Demand Inkjetting of Living Cell-Laden Bioink. *Langmuir* **2014** DOI: 10.1021/la501430x.

(45) Hockaday, L.; Kang, K. Rapid 3D printing of anatomically accurate and mechanically heterogeneous aortic valve hydrogel scaffolds. *Biofabrication* **2012**, *4* (3), 35005 DOI: 10.1088/1758-5082/4/3/035005.

(46) Song, S.-J.; Choi, J.; Park, Y.-D.; Hong, S.; Lee, J. J.; Ahn, C. B.; Choi, H.; Sun, K. Sodium alginate hydrogel-based bioprinting using a novel multinozzle bioprinting system. *Artif. Organs* **2011**, *35* (11), 1132–1136 DOI: 10.1111/j.1525-1594.2011.01377.x.

(47) Tan, Y.; Richards, D. J.; Trusk, T. C.; Visconti, R. P.; Yost, M. J.; Kindy, M. S.; Drake, C. J.; Argraves, W. S.; Markwald, R. R.; Mei, Y. 3D printing facilitated

scaffold-free tissue unit fabrication. *Biofabrication* **2014**, *6* (2), 24111 DOI: 10.1088/1758-5082/6/2/024111.

(48)   Duan, B.; Hockaday, L. a; Kang, K. H.; Butcher, J. T. 3D bioprinting of heterogeneous aortic valve conduits with alginate/gelatin hydrogels. *J. Biomed. Mater. Res. A* **2013**, *101* (5), 1255–1264 DOI: 10.1002/jbm.a.34420.

(49)   Schuurman, W.; Khristov, V.; Pot, M. W.; van Weeren, P. R.; Dhert, W. J. A.; Malda, J. Bioprinting of hybrid tissue constructs with tailorable mechanical properties. *Biofabrication* **2011**, *3* (2), 21001 DOI: 10.1088/1758-5082/3/2/021001.

(50)   Xu, T.; Binder, K. K. W.; Albanna, M. Z. M.; Dice, D.; Zhao, W.; Yoo, J. J.; Atala, A. Hybrid printing of mechanically and biologically improved constructs for cartilage tissue engineering applications. *Biofabrication* **2013**, *5* (1), 15001 DOI: 10.1088/1758-5082/5/1/015001.

(51)   Visser, J.; Peters, B.; Burger, T. Biofabrication of multi-material anatomically shaped tissue constructs. *Biofabrication* **2013**, *5* (3), 35007 DOI: 10.1088/1758-5082/5/3/035007.

(52)   Wei, C.; Cai, L.; Sonawane, B.; Wang, S.; Dong, J. High-precision flexible fabrication of tissue engineering scaffolds using distinct polymers. *Biofabrication* **2012**, *66* (3), 911–917.

(53)   Billiet, T.; Vandenhaute, M. A review of trends and limitations in hydrogel-rapid prototyping for tissue engineering. *Biomaterials* **2012**, *33* (26), 6020–6041 DOI: 10.1016/j.biomaterials.2012.04.050.

(54)   Vaezi, M.; Seitz, H.; Yang, S. A review on 3D micro-additive manufacturing technologies. *Int. J. Adv. Manuf. Technol.* **2013**, *67* (5–8), 1721–1754 DOI: 10.1007/s00170-012-4605-2.

(55)   Khalil, S.; Sun, W. Bioprinting endothelial cells with alginate for 3D tissue constructs. *J. Biomech. Eng.* **2009**, *131* (11), 111002 DOI: 10.1115/1.3128729.

(56)   Song, S.-J.; Choi, J.; Park, Y.-D.; Lee, J.-J.; Hong, S. Y.; Sun, K. A three-dimensional bioprinting system for use with a hydrogel-based biomaterial and printing parameter characterization. *Artif. Organs* **2010**, *34* (11), 1044–1048 DOI: 10.1111/j.1525-1594.2010.01143.x.

(57)   Cohen, D.; Malone, E. Direct freeform fabrication of seeded hydrogels in arbitrary geometries. *Tissue Eng.* **2006**, *12* (5), 1325–1335.

(58)   Mironov, V.; Reis, N.; Derby, B. Review: bioprinting: a beginning. *Tissue Eng.* **2006**, *12* (4), 631–634.

(59)   Kulkarni, R. K.; Moore, E. G.; Hegyeli, A. F.; Leonard, F. Biodegradable poly(lactic acid) polymers. *J. Biomed. Mater. Res.* **1971**, *5* (3), 169–181 DOI: 10.1002/jbm.820050305.

(60)   Giordano, R. A.; Wu, B. M.; Borland, S. W.; Cima, L. G.; Sachs, E. M.; Cima, M. J. Mechanical properties of dense polylactic acid structures fabricated by three dimensional printing. *J. Biomater. Sci. Polym. Ed.* **1996**, *8* (1), 63–75.

(61)   Chen, V. J.; Ma, P. X. Nano-fibrous poly(L-lactic acid) scaffolds with interconnected spherical macropores. *Biomaterials* **2004**, *25* (11), 2065–2073 DOI: 10.1016/j.biomaterials.2003.08.058.

(62)   Santamaría, V.; Deplaine, H. Influence of the macro and micro-porous structure on the mechanical behavior of poly (l-lactic acid) scaffolds. *J. Non. Cryst. Solids* **2012**, *358* (23), 3141–3149 DOI: 10.1016/j.jnoncrysol.2012.08.001.

(63)   Serra, T.; Mateos-Timoneda, M. A.; Planell, J. A.; Navarro, M. 3D printed PLA-based scaffolds. *Organogenesis* **2013**, *9* (4), 239–244 DOI: 10.4161/org.26048.

(64)   He, W.; Ma, Z.; Wee, E. T.; Yi, X. D.; Robless, P. A.; Thiam, C. L.; Ramakrishna, S. Tubular nanofiber scaffolds for tissue engineered small-diameter vascular

grafts. *J. Biomed. Mater. Res. - Part A* **2009**, *90* (1), 205–216 DOI: 10.1002/jbm.a.32081.

(65) Gregor, A.; Hošek, J. 3D Printing Methods of Biological Scaffolds Used in Tissue Engineering. In *Proceedings of International Conference On Innovations, Recent Trends and Challenges in Mechatronics, Mechanical Engineering And New High-Tech Products Development - MECAHITECH'11*; 2011; Vol. 3, pp 88–95.

(66) Loh, Q. L.; Choong, C. Three-dimensional scaffolds for tissue engineering applications: role of porosity and pore size. *Tissue Eng. Part B. Rev.* **2013**, *19* (6), 485–502 DOI: 10.1089/ten.TEB.2012.0437.

(67) Yang, J.; Shi, G.; Bei, J.; Wang, S.; Cao, Y.; Shang, Q.; Yang, G.; Wang, W. Fabrication and surface modification of macroporous poly (L-lactic acid) and poly (L-lactic-co-glycolic acid)(70/30) cell scaffolds for human skin fibroblast cell culture. *J. Biomed. Mater. Res.* **2002**, *62* (3), 438–446.

(68) Ma, P. X. Scaffolds for tissue fabrication. *Mater. Today* **2004**, *7* (5), 30–40 DOI: 10.1016/S1369-7021(04)00233-0.

(69) Hutmacher, D. W.; Sittinger, M.; Risbud, M. V. Scaffold-based tissue engineering: Rationale for computer-aided design and solid free-form fabrication systems. *Trends Biotechnol.* **2004**, *22* (7), 354–362 DOI: 10.1016/j.tibtech.2004.05.005.

(70) Varanasi, V. G.; Shiakolas, P. S.; Aswath, P. B. Engineered Scaffolds: Materials and Microstructure from Nanostructures to Macrostructures for Tissue Engineering. In *Scaffolds for Tissue Engineering: Biological Design, Materials, And Fabrication*; Migliaresi, C., Motta, A., Eds.; Pan Stanford Publishing Pte. Ltd.: Singapore, 2014; pp 435–519.

(71) Chia, H. N.; Wu, B. M. Recent advances in 3D printing of biomaterials. *J. Biol. Eng.* **2015**, *9*.

(72) Teoh, S. H.; Hutmacher, D. W.; Tan, K. C.; Tam, K. F.; Zein, I. Methods for fabricating a filament for use in tissue engineering. 2004.

(73) Hutmacher, D. W.; Schantz, T.; Zein, I.; Ng, K. W.; Teoh, S. H.; Tan, K. C. Mechanical properties and cell cultural response of polycaprolactone scaffolds designed and fabricated via fused deposition modeling. *J. Biomed. Mater. Res.* **2001**, *55* (2), 203–216.

(74) Bose, S.; Vahabzadeh, S.; Bandyopadhyay, A. Bone tissue engineering using 3D printing. *Mater. Today* **2013**, *16* (12), 496–504 DOI: 10.1016/j.mattod.2013.11.017.

(75) Welch, T. R.; Eberhart, R. C.; Chuong, C.-J. The influence of thermal treatment on the mechanical characteristics of a PLLA coiled stent. *J. Biomed. Mater. Res. B. Appl. Biomater.* **2009**, *90* (1), 302–311 DOI: 10.1002/jbm.b.31286.

(76) Welch, T. R.; Eberhart, R. C.; Reisch, J.; Chuong, C.-J. Influence of Thermal Annealing on the Mechanical Properties of PLLA Coiled Stents. *Cardiovasc. Eng. Technol.* **2014**, *5* (3), 270–280 DOI: 10.1007/s13239-014-0189-3.

(77) Lim, L.-T.; Auras, R.; Rubino, M. Processing technologies for poly(lactic acid). *Prog. Polym. Sci.* **2008**, *33* (8), 820–852 DOI: 10.1016/j.progpolymsci.2008.05.004.

(78) Hamad, K.; Kaseem, M.; Deri, F. Melt Rheology of Poly(Lactic Acid)/Low Density Polyethylene Polymer Blends. *Adv. Chem. Eng. Sci.* **2011**, *1* (4), 208–214 DOI: 10.4236/aces.2011.14030.

(79) Fang, Q.; Hanna, M. A. Rheological properties of amorphous and semicrystalline polylactic acid polymers. *Ind. Crops Prod.* **1999**, *10*, 47–53 DOI: 10.1016/S0926-6690(99)00009-6.

(80) Garlotta, D. A Literature Review of Poly (Lactic Acid). *J. Polym. Environ.* **2002**, *9* (2), 63–84 DOI: 10.1023/A:1020200822435.

(81) Turner, B. N.; Strong, R.; Gold, S. A. A review of melt extrusion additive manufacturing processes: I. Process design and modeling. *Rapid Prototyp. J.* **2014**, *20* (3), 192–204 DOI: 10.1108/RPJ-01-2013-0012.

(82) Ramanath, H. S.; Chua, C. K.; Leong, K. F.; Shah, K. D. Melt flow behaviour of poly-e-caprolactone in fused deposition modelling. *J. Mater. Sci. Mater. Med.* **2008**, *19* (7), 2541–2550 DOI: 10.1007/s10856-007-3203-6.

(83) Sengupta, R.; Chakraborty, S.; Bandyopadhyay, S.; Dasgupta, S.; Mukhopadhyay, R.; Auddy, K.; Deuri, a S. A Short Review on Rubber / Clay Nanocomposites With Emphasis on Mechanical Properties. *Engineering* **2007**, *47*, 21–25 DOI: 10.1002/pen.20921.

(84) Chen, Y.; Zhou, S.; Li, Q. Mathematical modeling of degradation for bulk-erosive polymers: Applications in tissue engineering scaffolds and drug delivery systems. *Acta Biomater.* **2011**, *7* (3), 1140–1149 DOI: 10.1016/j.actbio.2010.09.038.

(85) Yuan, X.; Mak, A. F. T.; Yao, K. Comparative observation of accelerated degradation of poly (L-lactic acid) fibres in phosphate buffered saline and a dilute alkaline solution. *Polym. Degrad. Stab.* **2002**, *75*, 45–53 DOI: https://doi.org/10.1016/S0141-3910(01)00203-8.

(86) Ratner, B. D.; Hoffman, A. S.; Schoen, F. J.; Lemons, J. E. *Biomaterials science: an introduction to materials in medicine*; 2004.

(87) Henton, D. E.; Gruber, P.; Lunt, J.; Randall, J. Polylactic Acid Technology. *Nat. Fibers, Biopolym. Biocomposites* **2005**, 527–578 DOI: 10.1201/9780203508206.ch16.

(88) Rezwan, K.; Chen, Q. Z.; Blaker, J. J.; Boccaccini, A. R. Biodegradable and bioactive porous polymer/inorganic composite scaffolds for bone tissue engineering. *Biomaterials* **2006**, *27* (18), 3413–3431 DOI: 10.1016/j.biomaterials.2006.01.039.

(89) Gong, Y.; Zhou, Q.; Gao, C.; Shen, J. In vitro and in vivo degradability and cytocompatibility of poly(l-lactic acid) scaffold fabricated by a gelatin particle leaching method. *Acta Biomater.* **2007**, *3* (4), 531–540 DOI: 10.1016/j.actbio.2006.12.008.

(90) Xiong, Z.; Yan, Y.; Zhang, R.; Sun, L. Fabrication of porous poly(L-lactic acid) scaffolds for bone tissue engineering via precise extrusion. *Scr. Mater.* **2001**, *45* (7), 773–779 DOI: 10.1016/S1359-6462(01)01094-6.

(91) Makadia, H. K.; Siegel, S. J. Poly Lactic-co-Glycolic Acid (PLGA) as Biodegradable Controlled Drug Delivery Carrier. *Polymers (Basel).* **2011**, *3* (3), 1377–1397 DOI: 10.3390/polym3031377.

(92) MacDonald, E.; Wicker, R. Multiprocess 3D printing for increasing component functionality. *Science (80-.).* **2016**, *353* (6307), 1512–1520.

(93) Wang, Y.; Ameer, G. A.; Sheppard, B. J.; Langer, R. A tough biodegradable elastomer. *Nat. Biotechnol.* **2002**, *20* (6), 602–606.

(94) Ochiai, Y.; Imoto, Y.; Sakamoto, M.; Kajiwara, T.; Sese, A.; Watanabe, M.; Ohno, T.; Joo, K. Mid-term follow-up of the status of Gore-Tex graft after extracardiac conduit Fontan procedure. *Eur. J. Cardio-thoracic Surg.* **2009**, *36* (1), 63–68.

(95) He, Y.; Tuck, C. J.; Prina, E.; Kilsby, S.; Christie, S. D. R.; Edmondson, S.; Hague, R. J. M.; Rose, F. R. A. J.; Wildman, R. D. A new photocrosslinkable polycaprolactone-based ink for three-dimensional inkjet printing. *J. Biomed. Mater. Res. - Part B Appl. Biomater.* **2017**, *105* (6), 1645–1657.

(96) Robotin, M. C.; Bruniaux, J.; Serraf, A.; Uva, M. S.; Roussin, R.; Lacour-Gayet, F.;

Planche, C. Unusual Forms of Tracheobronchial Compression in Infants with Congenital Heart Disease. *J. Thorac. Cardiovasc. Surg.* **1996**, *112* (2), 415–423.

(97) Austin, J.; Ali, T. Tracheomalacia and bronchomalacia in children: Pathophysiology, assessment, treatment and anaesthesia management. *Paediatr. Anaesth.* **2003**, *13* (1), 3–11.

(98) Vinograd, I.; Filler, R. M.; Bahoric, A. Long-term functional results of prosthetic airway splinting in tracheomalacia and bronchomalacia. *J. Pediatr. Surg.* **1987**, *22* (1), 38–41.

(99) Filler, R. M.; Buck, J. R.; Bahoric, A.; Steward, D. J. Treatment of segmental tracheomalacia and bronchomalacia by implantation of an airway splint. *J. Pediatr. Surg.* **1982**, *17* (5), 597–603.

(100) Blair, G. K.; Cohen, R.; Filler, R. M. Treatment of tracheomalacia: Eight years' experience. *J. Pediatr. Surg.* **1986**, *21* (9), 781–785.

(101) Zopf, D. A.; Hollister, S. J.; Nelson, M. E.; Ohye, R. G.; Green, G. E. Bioresorbable Airway Splint Created with a Three-Dimensional Printer. *N. Engl. J. Med.* **2013**, *368* (21), 2043–2045.

(102) Vinograd, I.; Klin, B.; Brosh, T.; Weinberg, M.; Flomenblit, Y.; Nevo, Z. A new intratracheal stent made from nitinol , an alloy with " shape memory effect ." *J. Thorac. Cardiovasc. Surg.* **1994**, *107* (5), 1255–1261.

(103) Carden, K. A.; Boiselle, P. M.; Waltz, D. A.; Enrst, A. Tracheomalacia and Tracheobronchomalacia in Children and Adults: An In-depth Review. *Chest* **2005**, *127* (3), 984–1005.

(104) Freitag, L.; Eicker, K.; Donovan, T.; Dimov, D. Mechanical properties of Airway Stents. *J. Bronchol.* **1995**, *2*, 270–278.

(105) Morrison, R. J.; Hollister, S. J.; Niedner, M. F.; Mahani, M. G.; Park, A. H.; Mehta, D. K.; Ohye, R. G.; Green, G. E. Mitigation of Tracheobronchomalacia with 3D-Printed Personalized Medical Devices in Pediatric Patients. *Sci. Transl. Med.* **2016**, *7* (285).

(106) Shieh, H. F.; Jennings, R. W. Three-dimensional printing of external airway splints for tracheomalacia. *J. Thorac. Dis.* **2017**, *9* (3), 414–416.

(107) Fraga, J. C.; Jennings, R. W.; Kim, P. C. W. Seminars in Pediatric Surgery Pediatric tracheomalacia. *Semin. Pediatr. Surg.* **2016**, *25* (3), 156–164.

(108) Welch, T. R.; Goodfriend, A. C.; Nair, A.; Thomas, C.; Veeram Reddy, S.; Nugent, A.; Guleserian, K.; Forbess, J. Bioresorbable Grafts for Congenital Heart Disease. In *The 6th International Conference on Mechanics of Biomaterials and Tissues*; Elsevier: Hawaii, 2015.

(109) Goodfriend, A. C.; Welch, T. R.; Nguyen, K. T.; Wang, J.; Johnson, R. F.; Nugent, A.; Forbess, J. M. Poly(gadodiamide fumaric acid): A Bioresorbable, Radiopaque, and MRI-Visible Polymer for Biomedical Applications. *ACS Biomater. Sci. Eng.* **2015**, *1* (8), 677–684.

(110) Welch, T. R.; Goodfriend, A. C. Biomimetic fluoroscopic films. WO2016191544 A1, 2016.

(111) G'sell, C.; Jonas, J. J. Determination of the plastic behaviour of solid polymers at constant true strain rate. *J. Mater. Sci.* **1979**, *14* (3), 583–591.

(112) Cvetkovic, C.; Raman, R.; Chan, V.; Williams, B. J.; Tolish, M.; Bajaj, P.; Sakar, M. S.; Asada, H. H.; Saif, M. T. a; Bashir, R. Three-dimensionally printed biological machines powered by skeletal muscle. *Proc. Natl. Acad. Sci. U. S. A.* **2014**, *111* (25), 10125–10130.

(113) Chen, Q. Z.; Bismarck, A.; Hansen, U.; Junaid, S.; Tran, M. Q.; Harding, S. E.; Ali, N. N.; Boccaccini, A. R. Characterisation of a soft elastomer poly(glycerol

sebacate) designed to match the mechanical properties of myocardial tissue. *Biomaterials* **2008**, *29* (1), 47–57.

(114) Kemppainen, J. M.; Hollister, S. J. Tailoring the mechanical properties of 3D-designed poly(glycerol sebacate) scaffolds for cartilage applications. *J. Biomed. Mater. Res. - Part A* **2010**, *94* (1), 9–18.

(115) Guan, J.; Fujimoto, K. L.; Sacks, M. S.; Wagner, W. R. Preparation and characterization of highly porous, biodegradable polyurethane scaffolds for soft tissue applications. *Biomaterials* **2005**, *26* (18), 3961–3971.

(116) Chan, V.; Zorlutuna, P.; Jeong, J. H.; Kong, H.; Bashir, R. Three-dimensional photopatterning of hydrogels using stereolithography for long-term cell encapsulation. *Lab Chip* **2010**, *10* (16), 2062–2070.

(117) Mazzoccoli, J. P.; Feke, D. L.; Baskaran, H.; Pintauro, P. N. Mechanical and cell viability properties of crosslinked low- And high-molecular weight poly(ethylene glycol) diacrylate blends. *J. Biomed. Mater. Res. - Part A* **2010**, *93* (2), 558–566.

(118) Ito, S.; Majumdar, A.; Kume, H.; Shimokata, K.; Naruse, K.; Lutchen, K. R.; Stamenovic, D.; Majumdar, A.; Kume, H.; Shi-, K.; et al. Viscoelastic and dynamic nonlinear properties of airway smooth muscle tissue : roles of mechanical force and the cytoskeleton. *Am. J. Physiol. Lung Cell Mol. Physiol.* **2006**, *290*, 1227–1237.

(119) Moroni, L.; Wijn, J. R. De; Blitterswijk, C. A. Van. 3D fiber-deposited scaffolds for tissue engineering : Influence of pores geometry and architecture on dynamic mechanical properties. *Biomaterials* **2006**, *27*, 974–985.

(120) Keim, T.; Gall, K. Synthesis, characterization, and cyclic stress-influenced degradation of a poly(ethylene glycol)-based poly(beta-amino ester). *J. Biomed. Mater. Res. - Part A* **2010**, *92* (2), 702–711.

(121) Rains, J. K.; Bert, J. L.; Roberts, C. R.; Paré, P. D. Mechanical properties of human tracheal cartilage. *J. Appl. Physiol.* **1992**, *72* (1), 219–225.

(122) Roberts, C. R.; Rains, J. K.; Pare, P. D.; Walker, D. C.; Wiggs, B.; Bert, J. L. Ultrastructure and tensile properties of human tracheal cartilage. **1998**, *31*, 81–86.

(123) Bandyopadhyay, A.; Bose, S.; Das, S. 3D printing of biomaterials. *MRS Bull.* **2015**, *40* (2), 108–115.

Biographical Information

Prashanth received his Honors BS in Mechanical Engineering *summa cum laude* from the University of Texas at Arlington (UTA) in May 2013. He joined the BS-PhD program in August 2013 and will be receiving his doctorate in December 2017. Prashanth has received many honors during his education at UTA, most notable of which include the Graduate Student Employee of the Year 2016-17, the Carizzo Oil & Gas Inc. Graduate Research Fellowship and the Igor Fraiberg Endowed Scholarship in Engineering. He has published multiple original research papers from his dissertation work in international journals and conference proceedings. Alongside his strong commitment to academics, Prashanth was also involved in extra-curricular activities with the Tau Beta Pi-Texas Eta, UTA Golden Key, the River Legacy Living Science Center and the Art of Living Meditation Club during his time at UTA. He also serves as a Peer Reviewer with the Journal of Manufacturing Science & Engineering (ASME) and Additive Manufacturing (Elsevier), and was invited to co-chair a session at the 2015 International Mechanical Engineering Congress & Exposition (IMECE) held in Houston, TX. He also served as a jugde at the 67th Fort Worth Regional Science and Engineering Fair as well as the yearly Honors Research Symposium at the UTA Honors College. After receiving his doctorate, Prashanth plans to work in the additive manufacturing area but intends to stay involved with research activities in his role as Peer Reviewer as well as via continued collaboration on research projects with his doctoral advisor. His ultimate ambition is to start a company and employ the proceeds towards creating scholarship endowments at his alma mater to help deserving students complete their education.